JCB Journal of Cell Biology

ARTICLE

Multivalent weak interactions between assembly units drive synaptonemal complex formation

Zhenguo Zhang[1*], Songbo Xie[1*], Ruoxi Wang[1*], Shuqun Guo[1], Qiuchen Zhao[1], Hui Nie[1], Yuanyuan Liu[1], Fengguo Zhang[1], Miao Chen[1], Libo Liu[1], Xiaoqian Meng[1], Min Liu[1], Li Zhao[2,3], Monica P. Colaiácovo[4], Jun Zhou[1,5], and Jinmin Gao[1]

The synaptonemal complex (SC) is an ordered but highly dynamic structure assembled between homologous chromosomes to control interhomologous crossover formation, ensuring accurate meiotic chromosome segregation. However, the mechanisms regulating SC assembly and dynamics remain unclear. Here, we identified two new SC components, SYP-5 and SYP-6, in *Caenorhabditis elegans* that have distinct expression patterns and form distinct SC assembly units with other SYPs through stable interactions. SYP-5 and SYP-6 exhibit diverse in vivo SC regulatory functions and distinct phase separation properties in cells. Charge-interacting elements (CIEs) are enriched in SC intrinsically disordered regions (IDRs), and IDR deletion or CIE removal confirmed a requirement for these elements in SC regulation. Our data support the theory that multivalent weak interactions between the SC units drive SC formation and that CIEs confer multivalency to the assembly units.

Introduction

Paired homologous chromosomes are stabilized during meiosis by a proteinaceous macromolecular structure known as the synaptonemal complex (SC). This allows for interhomologue recombination and formation of crossovers (COs), providing physical attachments between homologous chromosomes for their proper alignment and subsequent segregation. Although it has been 60 yr since this protein structure was identified, the mechanisms underlying its assembly and dynamics remain unclear.

Electron microscopy reveals that the fully formed SC is ultrastructurally conserved and consists of two lateral elements and a central region with widths of 90–150 nm between species (Moses, 1969). While SC components do not show obvious sequence similarity across organisms, the organization of central region components is conserved, comprising transverse filaments (TFs) and central elements in most organisms. The TFs are organized in a head-to-head orientation with their N termini located in the middle of the central region and the C termini facing the chromosome axes (reviewed by Cahoon and Hawley, 2016; Gao and Colaiácovo, 2018). The central element proteins overlap with the N termini of the TF proteins, stabilizing the SC. Despite its highly organized structure, the SC is not static, and its components consistently come on and off from chromosomes during early prophase. This dynamic behavior is thought to be essential for its function in regulating meiotic recombination and CO formation (Nadarajan et al., 2017; Pattabiraman et al., 2017; Voelkel-Meiman et al., 2012). Moreover, the SC has been reported to exhibit a liquid crystalline property that may underlie CO regulation (Rog et al., 2017; Zhang et al., 2018). Interestingly, SC central region proteins usually contain coiled-coil domains and intrinsically disordered regions (IDRs). While the former are known to mediate interactions between SC components (Davies et al., 2012; Dunce et al., 2018; Schild-Prüfert et al., 2011), the role of IDRs in SC assembly and dynamics remains enigmatic. During late meiotic prophase, SC components were found to remain associated with chromosome subdomains in diverse organisms (Bisig et al., 2012; Gladstone et al., 2009; Nabeshima et al., 2005; Newnham et al., 2010; Qiao et al., 2012; Takeo et al., 2011); however, the molecular consequences for such retention are not clear. In *Caenorhabditis elegans*, although asymmetric SC disassembly accompanies chromosome remodeling and the establishment of bivalent asymmetry required for their accurate segregation (de Carvalho et al., 2008; Martinez-Perez et al., 2008; Sato-Carlton et al., 2018; Tzur et al., 2012), the requirement for the maintenance of SC components during this process is not known.

In this study, we identified two novel SC proteins, SYP-5 (ORF Y54E10A.12) and SYP-6 (ORF F57B10.4), whose genes are

[1]Institute of Biomedical Sciences, College of Life Sciences, Key Laboratory of Animal Resistance Biology of Shandong Province, Shandong Normal University, Jinan, Shandong, China; [2]Department of Pathology, Harvard Medical School, Dana-Farber/Harvard Cancer Center, Boston, MA; [3]Department of Laboratory Medicine, Children's Hospital Boston, Boston, MA; [4]Department of Genetics, Harvard Medical School, Boston, MA; [5]State Key Laboratory of Medicinal Chemical Biology, College of Life Sciences, Nankai University, Tianjin, China.

*Z. Zhang, S. Xie, and R. Wang contributed equally to this paper; Correspondence to Jinmin Gao: jinmingao@sdnu.edu.cn; Jun Zhou: junzhou@sdnu.edu.cn.

201910086predicted paralogs. Null mutants for *syp-5* and *syp-6* exhibit opposite effects in SC loading compared with wild type, and *syp-5 syp-6* double mutants show phenotypes similar to previously characterized *syp* null mutants, suggesting that SYP-5 and SYP-6 have redundant roles, but distinct properties, in SC regulation. The *syp-5* null mutant does not show a significant effect on CO formation but results in premature SC disassembly, providing an ideal tool to explore the biological significance of SC maintenance during late prophase. In vivo and in vitro interaction analyses revealed that SYP-5 and SYP-6 form distinct SC assembly units with other SYPs through stable interactions, suggesting that weak interactions between these units drive SC formation. We further demonstrated the pervasiveness of charge-interacting elements (CIEs) among SC components and their essential role in SC regulation.

Results

SYP-5 and SYP-6 are novel SC-associated proteins

To better understand the mechanisms involved in SC regulation, we used a proteomic approach to identify SC-associated proteins in *C. elegans*. Immunoprecipitation (IP) of the SC central region protein, SYP-2, followed by mass spectrometry (MS) analysis identified two coiled-coil domain-containing proteins, SYP-5 and SYP-6, as novel SC-associated proteins (Fig. 1, A and B; and Fig. S1 A). These two proteins share conserved sequences, and their genes are predicted paralogs. Moreover, their in vivo translation rates were similar to those of other SYPs (Fig. S1 B; Tzur et al., 2018).

To clarify the roles of SYP-5 and SYP-6 in meiosis, null mutants of the corresponding genes were generated by the CRISPR-Cas9 method (Fig. S2). Compared with wild type, *syp-5* single mutants had higher rates of embryonic lethality ([Emb] 20.2%) and high incidence of male (Him) progeny (9.8%), which can be indicative of impaired meiotic chromosome segregation. On the other hand, *syp-6* mutants showed a mild phenotype (Emb, 0.8%; Him, 1.2%; Fig. 1 C). Interestingly, extremely high rates of Emb (96.6%) and Him (36.1%) were observed in *syp-5 syp-6* double mutants, similar to the phenotype of mutants lacking the SC (Colaiácovo et al., 2003; Smolikov et al., 2007, 2009; Fig. 1 C). These observations indicate that SYP-5 and SYP-6 have partly redundant roles and they do not function equally during meiosis.

syp-5 and *syp-6* exhibit opposite effects in SC loading during early prophase

To determine whether meiotic chromosome synapsis is affected in *syp-5* or *syp-6* mutants, the *syp-2::gfp* transgene was introduced into these mutants to visualize the SC. Delayed and incomplete chromosome synapsis was observed in *syp-5* mutants (Fig. 1 E; and Fig. S3, A and B). A subset of chromosomes in nuclei located in the region of the germline corresponding to mid-pachytene in wild type lacked the SC in *syp-5* mutants, and chromosomes remained clustered in a similar crescent-shaped organization as observed in leptotene/zygotene nuclei upon meiotic entry (Fig. 1 E). In contrast, no obvious defects in synapsis were observed in *syp-6* mutants (Fig. 1 E). In *syp-5 syp-6* double mutants, the SC was no longer detected (Fig. 1 F and Fig. S3 C). These observations suggest that SYP-5 and SYP-6 may have a redundant role in SC formation.

An overall weak SYP-2::GFP fluorescence signal was observed in nuclei at meiotic prophase in *syp-5* mutants (Fig. 1 E and Fig. S3 D), indicating impaired accumulation of SC components on the linear SC structure between homologous chromosomes (referred to as SC loading). To evaluate SC loading more precisely in different genetic backgrounds, we measured the total fluorescence intensity for SYP-2::GFP in meiotic prophase nuclei (Fig. 1 G). Interestingly, SC loading was reduced in *syp-5* mutants but enhanced in *syp-6* mutants (Fig. 1 H), providing evidence for the distinct properties of these proteins in SC regulation.

SYP-5 is required for SC maintenance in late prophase

To further determine the source of errors resulting in the increased Emb in *syp-5* mutants, we examined meiotic events at different stages (Fig. 2 A). At the end of meiotic prophase, wild-type *C. elegans* had six DAPI-stained bodies per nucleus, corresponding to six pairs of attached homologous chromosomes. In *syp-5* mutants, most nuclei (87%) also contained six DAPI-stained bodies, and only a small portion (13%) had seven, implying a relatively low frequency of univalents at diakinesis (Fig. 2 B). Univalent formation is unlikely to be the main cause of the high Emb and Him rates in *syp-5* mutants, given that a pair of autosomes consistently left unpaired in *zim-2* mutants gave high Emb (~30%) but mild Him (1%; Phillips and Dernburg, 2006) and unpaired X chromosomes in *him-8* mutants gave only high Him (40%) but no Emb (Phillips et al., 2005). No defect in bivalent formation was detected in *syp-6* mutants. However, most diakinesis nuclei (80%) of *syp-5 syp-6* double mutants harbored 10–12 DAPI-stained bodies (Fig. 2 B), consistent with the functional redundancy of SYP-5 and SYP-6 in synapsis and bivalent formation.

Analysis of the CO-designation marker COSA-1/CNTD1 (Holloway et al., 2014; Yokoo et al., 2012) during the late pachytene stage showed generally normal CO control in both *syp-5* and *syp-6* mutants; six GFP::COSA-1 foci were observed in most nuclei, with one focus on each chromosome (Fig. 2, C–E). However, defects in SC disassembly were observed in these mutants. In wild type, asymmetric SC disassembly takes place upon pachytene exit and SYP proteins are retained on the bivalent short arms until late diakinesis (Nabeshima et al., 2005). Strikingly, the association of SC proteins on chromosomes was completely lost upon pachytene exit in *syp-5* mutants (Fig. 2 F), suggesting that SYP-5 is critical for maintaining the SC proteins on chromosomes during late meiotic prophase. In *syp-6* mutants, although SC proteins still aggregated toward one end of each chromosome, these proteins also remained associated on the remaining parts of the chromosomes (Fig. 2 F). Despite this defect, as in wild type, SC central region proteins no longer associated with the bivalents at the end of meiotic prophase in *syp-6* mutants (Fig. 2 G). Defects in SC disassembly may explain the Emb and Him phenotypes observed in *syp-5* and *syp-6* single mutants.

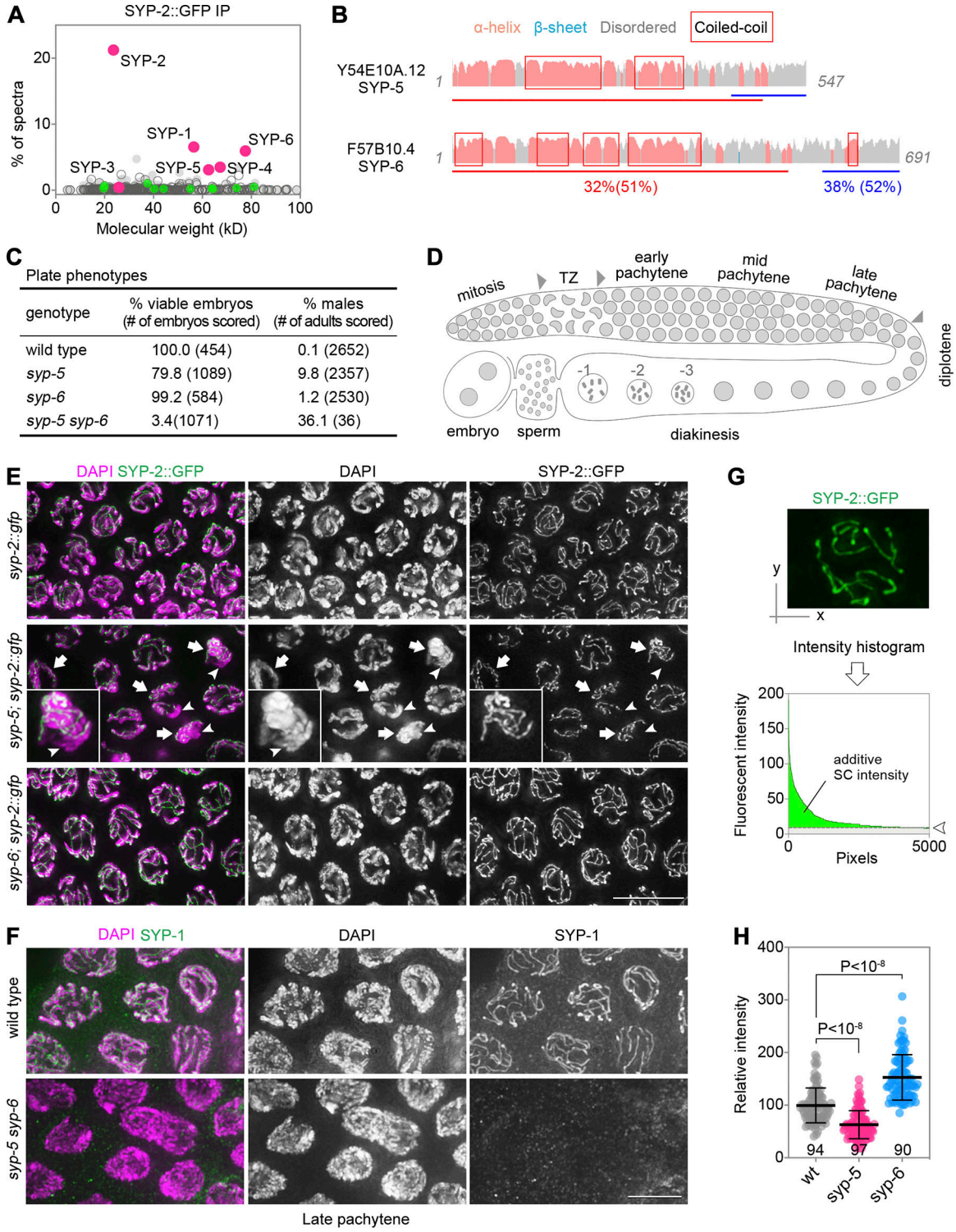

Figure 1. **SYP-5 and SYP-6 are novel SC-associated components with distinct SC regulatory properties. (A)** MS identification of SYP-5 and SYP-6 by IP of SYP-2::GFP. Circles and gray dots represent proteins identified from SYP-2::GFP and control immunoprecipitates, respectively; SYPs and other proteins specifically identified in SYP-2::GFP IPs are shown in red and green, respectively. Data represent the mean value from three biological replicates. **(B)** Secondary protein structure of SYP-5 and SYP-6. Lines of the same color represent regions of homology; amino acid identity and similarity (in parentheses) are indicated. **(C)** Plate phenotypes of *syp-5*, *syp-6*, and *syp-5 syp-6* mutants. **(D)** Schematic of meiotic prophase substages in the *C. elegans* germline. Arrowheads indicate transitions between substages: meiotic entry, where TZ corresponds to leptotene/zygotene, pachytene entry, and pachytene exit. **(E)** SYP-2::GFP (green) localization in nuclei of the indicated genotypes. Incomplete synapsis (arrowheads) and nuclei with chromosomes in a crescent-shaped configuration (arrows) were observed in *syp-5* mutants in the region corresponding to the mid-pachytene in wild type. A representative nucleus with incomplete synapsis is shown at higher magnification in insets for *syp-5* mutants. Bar, 10 µm. **(F)** SYP-1 (green) was not detected in pachytene nuclei of *syp-5 syp-6* double mutants by immunostaining. Chromatin was stained with DAPI (magenta). Bar, 5 µm. **(G)** Quantification of SYP-2::GFP loading in pachytene nuclei. Maximum-intensity

projection of 3D data stacks of the whole nuclear SYP-2::GFP signal was first generated (top), and additive fluorescent signal above the background of this 2D image was further measured for each nucleus (bottom, green area). Total signal intensity was normalized to the background signal (open arrowhead) before being used for comparison. **(H)** *syp-5* and *syp-6* mutants exhibit opposite effects on SYP-2::GFP loading in mid-pachytene nuclei. Bars represent the mean ± SD of normalized SYP-2::GFP fluorescent intensities; numbers of nuclei measured for each genotype are indicated. Measurements were performed as in G, and two-tailed unpaired *t* test was performed for statistical analysis. wt, wild type.

SYP-5 is required for bivalent remodeling in late prophase

Chromosome remodeling involves redistribution of chromosome-associated proteins during late prophase and results in long arm association of LAB-1 and HTP-1/2 and short arm localization of aurora B kinase AIR-2 (de Carvalho et al., 2008; Ferrandiz et al., 2018; Martinez-Perez et al., 2008; Nabeshima et al., 2005; Sato-Carlton et al., 2018; Tzur et al., 2012; Zhang et al., 2018). AIR-2 activity is required for the dissolution of short arm sister chromatid cohesion, thus defining the chromosome segregation pattern. GFP::AIR-2 was observed localizing to the short arms of bivalents in -1 oocytes in wild type; however, this was not observed in the *syp-5* mutant background (Fig. 3 A). Phosphorylation of histone H3 (pH3) at Ser10 by AIR-2 (Hsu et al., 2000) can serve as an indicator of AIR-2 kinase activity.

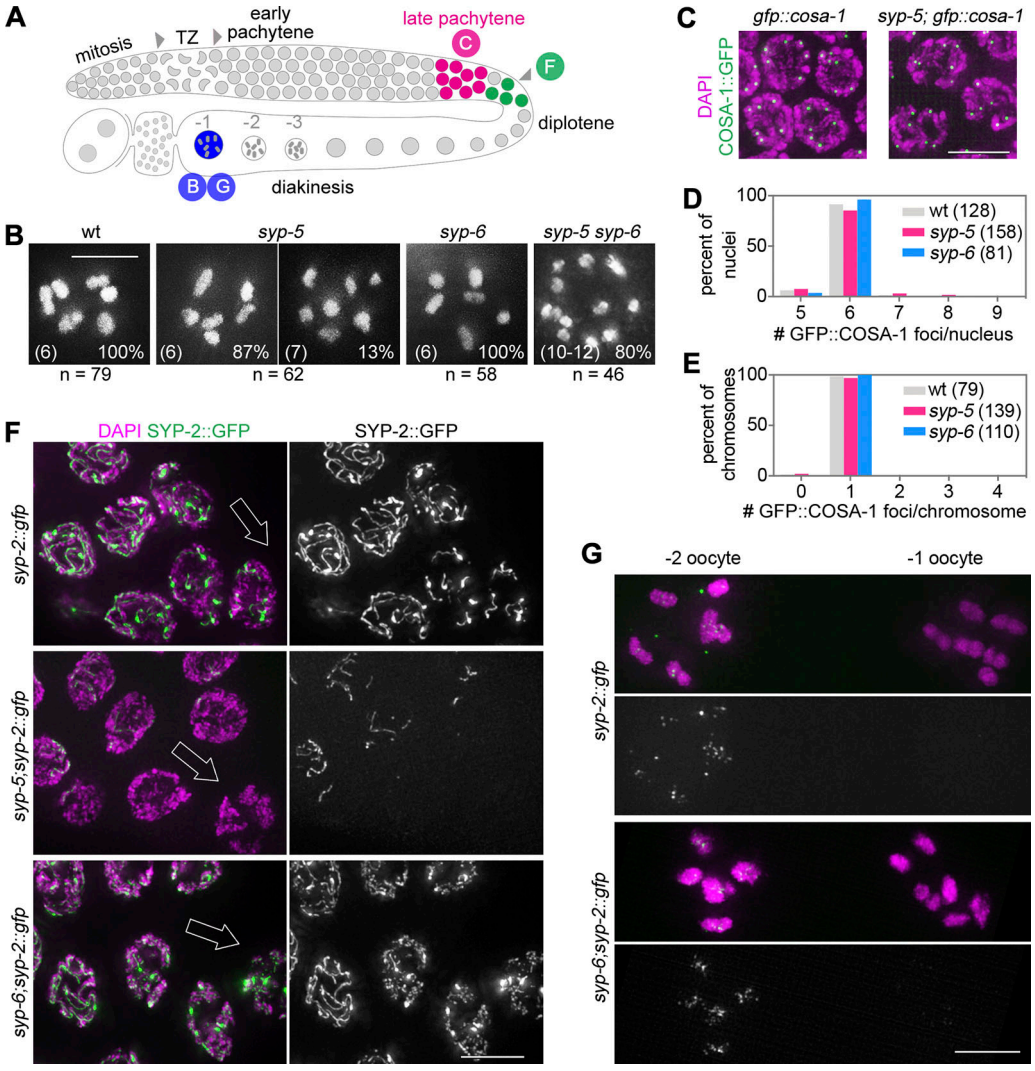

Figure 2. **SYP-5 is required for maintenance of SC proteins on chromosome subdomains in late prophase. (A)** Schematic of meiotic progression in the *C. elegans* germline with regions colored as follows: red, late pachytene stage; green, pachytene exit; and blue, -1 oocyte. The letters C, F, B, and G refer to other panels in the figure. **(B)** DAPI-stained bodies in -1 oocytes at diakinesis in the indicated genotypes. The number of observed DAPI-stained bodies is indicated in parentheses. Bar, 5 µm. **(C)** Formation of GFP::COSA-1 foci (green) in late pachytene nuclei from indicated genotypes. Chromatin was stained with DAPI (magenta). Bar, 5 µm. **(D and E)** Quantification of GFP::COSA-1 foci in indicated genotypes. Numbers of nuclei or chromosomes scored are indicated. **(F)** SC (marked by SYP-2::GFP, green) disassembly process in the indicated genotypes. Chromatin was stained with DAPI (magenta). Open arrows indicate orientation of meiotic progression from late pachytene into diplotene. Bar, 5 µm. **(G)** SYP-2::GFP (green) disappears at the end of meiotic prophase (-1 oocyte) in the *syp-6* mutant background. Chromatin was stained with DAPI (magenta). Bar, 5 µm. wt, wild type.

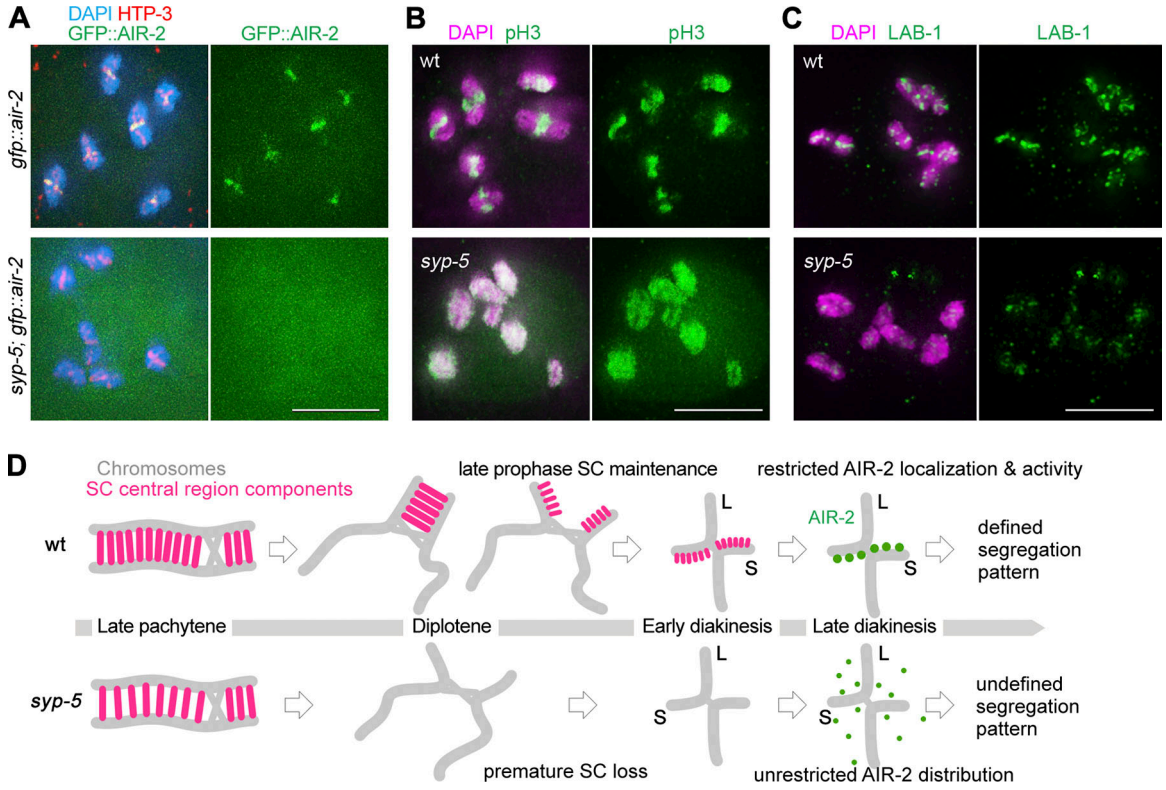

Figure 3. **SYP-5 is required for proper chromosome remodeling in late prophase. (A)** Immunostaining for the chromosome axis marker HTP-3 (red) in -1 oocytes of the indicated genotypes that express GFP::AIR-2 (green). Chromatin was stained with DAPI (blue). Bar, 5 µm. **(B)** Immunostaining for Ser10 pH3 (green) in -1 oocytes of indicated genotypes. Chromatin was stained with DAPI (magenta). Bar, 5 µm. **(C)** Immunostaining for LAB-1 (green) in -1 oocytes of indicated genotypes. Chromatin was stained with DAPI (magenta). Bar, 5 µm. **(D)** Schematic illustration of the requirement for short arm association of SC central region components during late meiotic prophase for proper bivalent remodeling and segregation. L, long arm; S, short arm; wt, wild type.

Consistent with the GFP::AIR-2 localization pattern, the pH3 signal was restricted to bivalent short arms in -1 oocytes in wild type but was detected throughout the chromosomes in *syp-5* mutants (Fig. 3 B). Chromosome association of LAB-1 was also reduced in *syp-5* mutants (Fig. 3 C), contributing to the abnormal pH3 distribution. Collectively, as shown by Sato-Carlton et al. (2018), these data highlight the roles of SC central region components in mediating bivalent remodeling during late prophase (Fig. 3 D).

SYP-5 and SYP-6 colocalize with the SC and exhibit distinct expression patterns

To investigate the localization and expression patterns of SYP-5 and SYP-6, a GFP tag was inserted at the end of the coding sequences of endogenous *syp-5* and *syp-6* (Fig. S2). No Emb phenotype was observed for *syp-5::gfp* and *syp-6::gfp* worms (Fig. S2 D), suggesting that these tagged genes are functional. The expression of SYP-5 and SYP-6 was germline specific, and they exhibited distinct expression patterns. SYP-5::GFP reached its highest expression level at the end of the pachytene stage, while SYP-6::GFP exhibited strong expression before late pachytene (Fig. 4 A). Moreover, the expression pattern of endogenous SYP-5 was similar to that observed for SYP-5::GFP, as evaluated with a SYP-5–specific antibody (Fig. S4). Super-resolution structured illumination microscopy (SIM) analysis showed that both SYP-5::GFP and SYP-6::GFP located at the central region of the SC, where they were clearly flanked by the axis-associated HTP-3 (Fig. 4 B). While SYP-6::GFP was detected only during early prophase (until late pachytene), SYP-5::GFP colocalized with the SC throughout the meiotic prophase, and its signal disappeared by the end of diakinesis (Fig. 4 C). By normalizing fluorescence signal intensities for different SYPs according to their levels at the mid-pachytene stage, we found that SYP-5::GFP loading was significantly lower than the other SYPs during early prophase (transition zone [TZ] and early pachytene), whereas SYP-6::GFP loading was lower than the other SYPs during late pachytene (Fig. 4 D). These observations indicate that the composition of the SC varies during meiotic progression.

In *syp-1* null mutants lacking the SC central region, chromosome association of SYP-5::GFP was no longer observed (Fig. 4 E), consistent with the interdependence between SYPs for their chromosome loading. Interestingly, compared with wild type, an increased SYP-5 fluorescence signal was observed during early meiotic prophase (TZ) in *syp-6* mutants, suggesting an inhibitory effect on SYP-5 loading by SYP-6 during early meiotic prophase (Fig. S4 C).

SYP-5 and SYP-6 form distinct SC assembly units

To dissect the SC protein interaction network, in vivo complex formation was assessed by IP and MS (Fig. 5, A–C). SYP-5::GFP

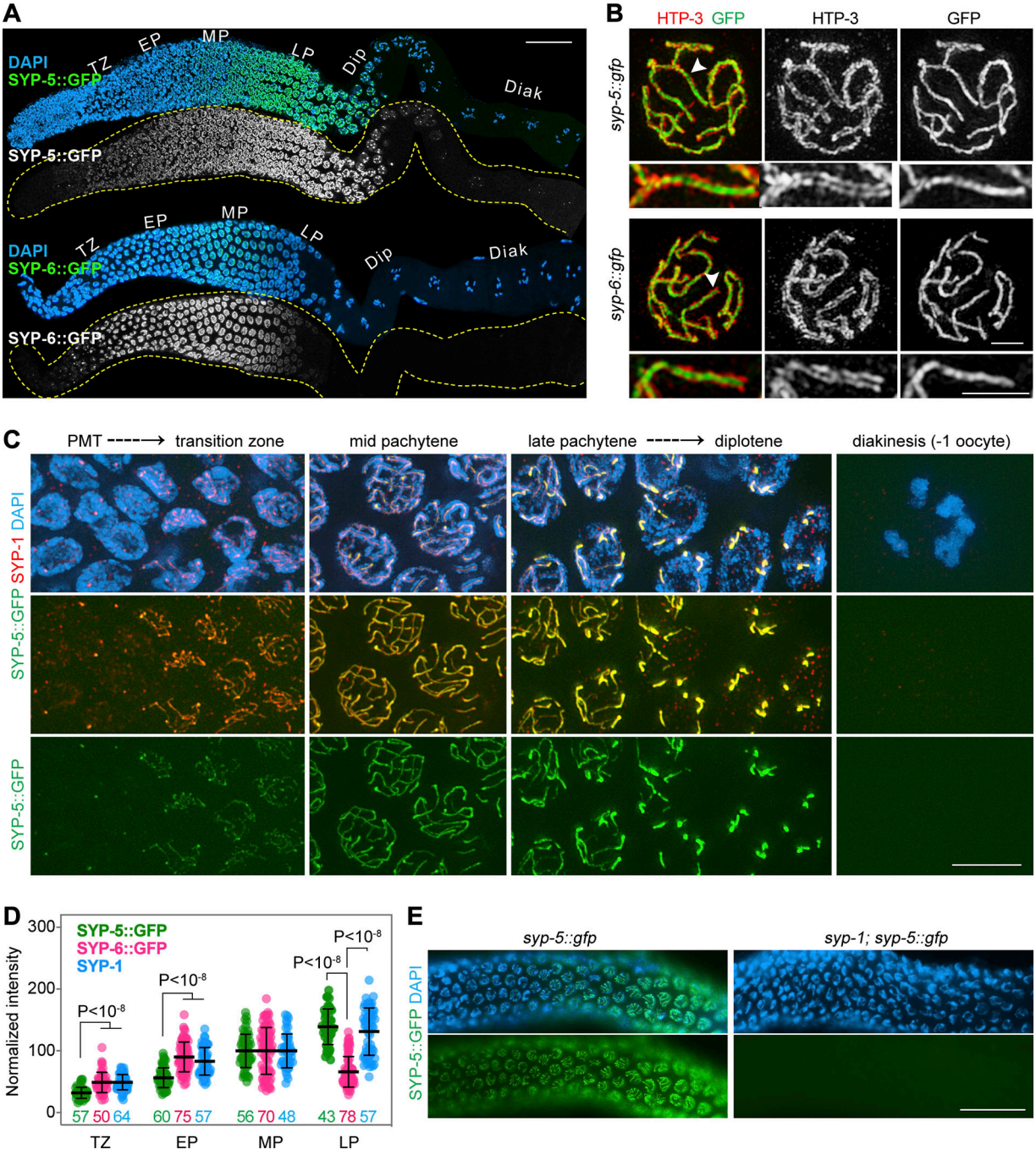

Figure 4. **SYP-5 and SYP-6 exhibit distinct expression patterns during meiotic prophase. (A)** Expression patterns of endogenously tagged SYP-5 and SYP-6 (green) in the germline. Yellow dashed lines depict the outlines of the gonads. Chromatin was stained with DAPI (blue). Diak, diakinesis; Dip, diplotene; EP, early pachytene; LP, late pachytene; MP, mid-pachytene. Bar, 30 µm. **(B)** SIM analysis of SYP-5::GFP and SYP-6::GFP (green) localization in pachytene nuclei. The meiotic chromosome axis was visualized by immunostaining of HTP-3 (red). Bar, 2 µm. White arrowheads indicate the SC stretches shown at a higher magnification at the bottom. **(C)** Immunostaining for SYP-1 (red) in *syp-5::gfp* germline cells. Yellow stretches indicate the colocalization of SYP-5::GFP (green) with SYP-1. Chromatin was stained with DAPI (blue). Bar, 5 µm. PMT, premeiotic tip. **(D)** Measurement of SYP protein loading from TZ through late pachytene. Signal intensity for different SYPs at different stages was normalized according to the mean values at mid-pachytene stage. Bars represent the mean ± SD of normalized GFP fluorescent intensities. Measurements were performed as in G; numbers of nuclei measured for each stage are indicated, and two-tailed unpaired *t* test was performed for statistical analysis. **(E)** The SC is required for association of SYP-5::GFP (green) with chromosomes. Gonads dissected from indicated genotypes were fixed and stained with DAPI (blue). Bar, 20 µm.

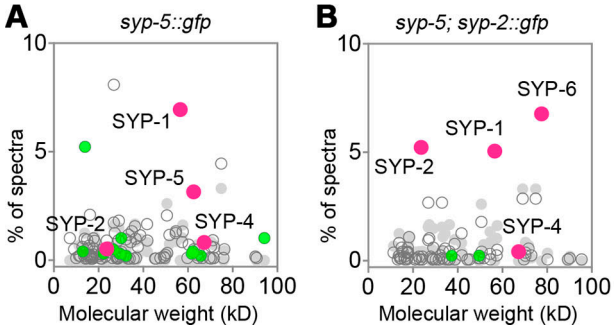

C

% of spectra

Genotype	*syp-2::gfp*	*syp-5::gfp*	*syp-5; syp-2::gfp*
SYP-1	6.6	6.9	5.1
SYP-2	21.2	0.5	5.2
SYP-3	0.4	ND	ND
SYP-4	3.5	0.8	0.4
SYP-5	3.1	3.2	ND
SYP-6	6.0	ND	6.8

Figure 5. **IP and MS analyses of SYP-binding proteins in vivo. (A)** MS identification of SYP-5::GFP binding partners in vivo. Circles and gray dots represent proteins identified from SYP-5::GFP and control immunoprecipitates, respectively; SYPs and other proteins specifically identified in SYP-5::GFP IPs are highlighted in red and green, respectively. Data represent the mean value from two independent replicates. **(B)** MS identification of SYP-2::GFP binding partners in a *syp-5* mutant background. Data represent the mean value of two independent replicates. **(C)** Summary of MS data for SYP proteins in different genetic backgrounds. ND, not detected; red ND, absence of SYP-6 in SYP-5::GFP immunoprecipitates.

IP yielded three SYP proteins (SYP-1, -2, and -4) as binding partners (Fig. 5 A). SYP-3 was not detected in the immunoprecipitates, possibly due to its small size (224 aa) and poor peptide coverage with trypsin digestion. Interestingly, although SYP-6 peptides were abundant in SYP-2::GFP immunoprecipitates, no SYP-6 peptide was detected in association with SYP-5::GFP (Fig. 5 C). This implies that SYP-5 and SYP-6 form distinct SC assembly units that do not engage in a stable interaction. This was supported by the fact that complex formation between SYP-1, SYP-2, SYP-4, and SYP-6 was unaffected when IP of SYP-2::GFP was performed in the *syp-5* mutant background (Fig. 5, B and C).

To further map the SC interaction network, constructs expressing full-length and truncated forms of different SYPs were coexpressed in mammalian 293T cells, and protein interactions were evaluated by IP and Western blotting (Fig. 6, A–H). SYP-1 and SYP-3 were found to interact with both SYP-5 and SYP-6 (Fig. 6, B and C); however, no interaction was detected between SYP-5 and SYP-6 (Fig. 6 B). SYP-1 and SYP-5 mainly interacted through their coiled-coil regions (Fig. 6, D and E), although a relatively weak interaction was also detected between full-length SYP-1 and the C terminus of SYP-5 (Fig. 6 D). On the contrary, SYP-5 associated with SYP-3 through its N terminus (Fig. 6 F). Interestingly, SYP-6 was observed to interact with other SYPs in a manner similar to SYP-5. SYP-6 associated with SYP-1 and SYP-3 through its central coiled-coil region (Fig. 6 G) and its N terminus (]Fig. 6 H), respectively. These results, along with previously described interaction patterns (Schild-Prüfert et al., 2011), suggest that coiled-coil domain–mediated interactions are critical for the formation of SC assembly units. Moreover, with combined tools, we also detected self-interactions of the central coiled coils of SYP-1, SYP-5, and SYP-6 (Fig. 6, I–K), suggesting the dimerization of these components within the units. The similar manner in which SYP-5 and SYP-6 associate with other SYPs suggests competitive binding but also formation of distinct SC assembly units (Fig. 6 L).

SYP-5 and SYP-6 exhibit distinct phase separation properties in cells

To further explore how SYPs may cooperate in SC formation, fluorescent-tagged SYP proteins were expressed in 293T cells. SYP-1, SYP-3, SYP-5, and SYP-6 were found to form aggregates, while aggregates with SYP-2 and SYP-4 were not observed (Fig. 7 A). Aggregates formed by different SYPs also differed, and SYP-5 was frequently observed forming a large droplet-like structure, representing a phase-separated structure (Fig. 7 A). To better characterize the SYP aggregates, their areas and perimeters were measured (Fig. 7, B and C). The ratio between measured perimeters ($C_{measured}$) and calculated perimeters of the equivalent circular areas (C_{circle}) represents the extent to which the aggregates resembled round droplets (referred to as phase separation trend analysis). Compared with other SYPs, SYP-5 exhibited the lowest $C_{measured}/C_{circle}$ ratio (Fig. 7 D), suggesting that SYP-5 may function as the primary driver of phase separation among the SYPs. Moreover, live cell imaging also revealed different levels of dynamics for the SYP aggregates. Fusion of SYP-5 aggregates was observed, while such fusion process was not observed with other SYPs in the same time window (Fig. 7 E).

To test how SYP-5 and SYP-6 can affect the behavior of SC assembly units, we performed a simplified, two-component coexpression analysis with SYP-1 and SYP-3, which can also form aggregates and were found to interact with SYP-5 and SYP-6. Not surprisingly, SYP-5 and SYP-6 were found to colocalize with SYP-1 and SYP-3 aggregates (Fig. 7, F and H). Phase separation trend analysis indicated a stronger promoting role of SYP-5 on both SYP-1 and SYP-3 than that of SYP-6. (Fig. 7, G and I). Consistently, live cell imaging showed that SYP-3 and SYP-5 coexpression resulted in the fusion of their aggregates, although such fusion process was not obvious for SYP-1/SYP-5 aggregates (Fig. 7 J).

SC components are enriched in CIEs

SC proteins from various organisms are predicted to harbor a large fraction of IDRs among their sequences (Gao and Colaiacovo, 2017). Numerous studies have also demonstrated the involvement of IDRs in phase separation, and specific types of amino acids can form short linear interaction motifs within the IDRs (reviewed in Boeynaems et al., 2018). IDR-mediated multivalent interactions between SC assembly units could drive SC formation in a manner akin to phase separation and confer a

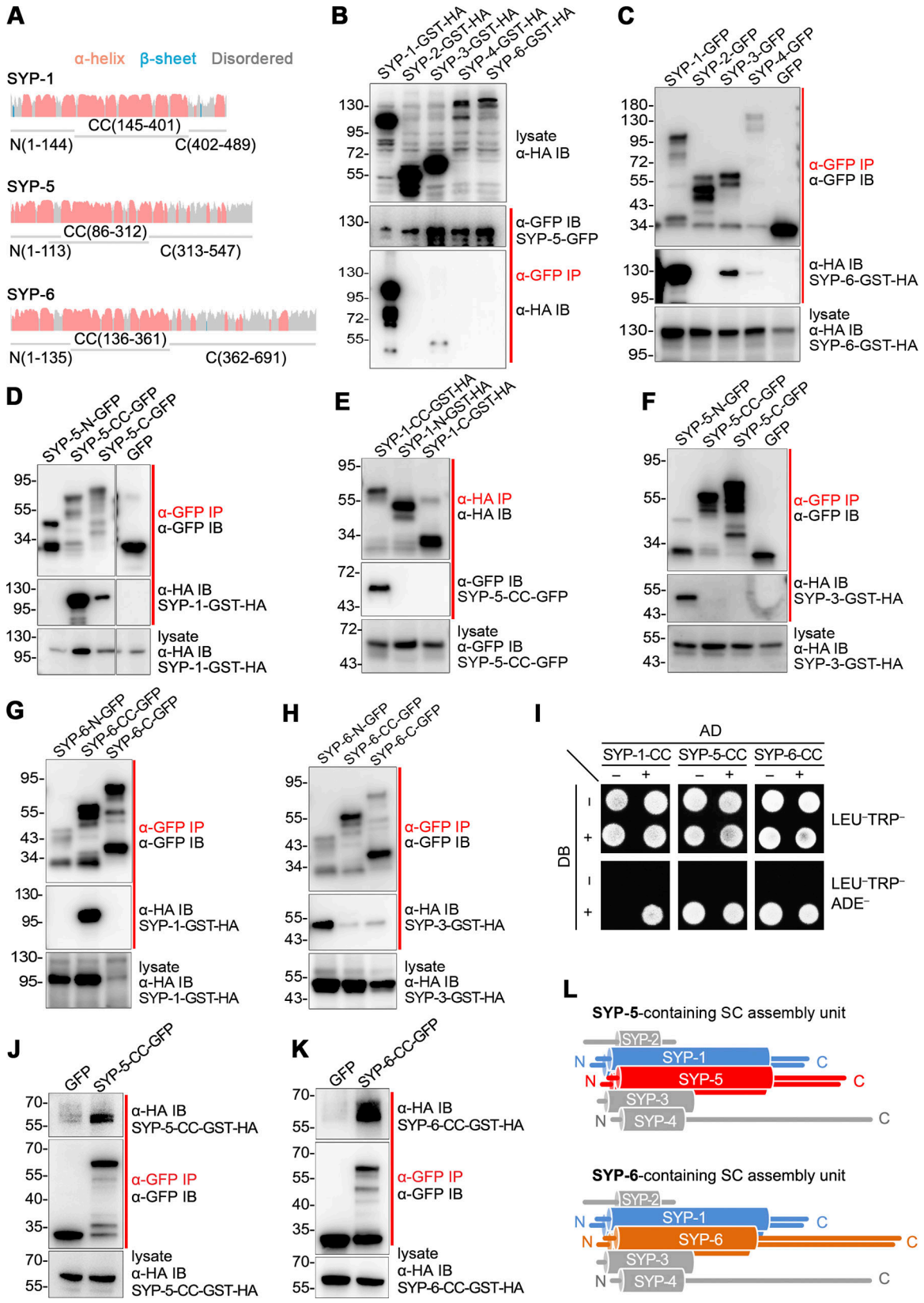

Figure 6. **In vitro mapping of interactions between SC components. (A)** Truncated forms of SYPs used to map the SC interaction network in this study are depicted by the gray horizontal lines. Amino acid boundaries are indicated. C, C terminus; CC, central coiled-coil region; N, N terminus. **(B–H)** SYP proteins expressed in 293T cells were mapped for their interactions by IP and immunoblot (IB) analysis. Red vertical lines indicate IB analysis of IP samples. **(B)** Full-length SYP-5 interacted with SYP-1 and SYP-3. **(C)** Full-length SYP-6 interacted with SYP-1 and SYP-3. **(D)** The coiled-coil region and C terminus of SYP-5 interacted with SYP-1. **(E)** SYP-1 and SYP-5 interacted through their coiled-coil regions. **(F)** The N terminus of SYP-5 interacted with SYP-3. **(G)** The coiled-coil

region of SYP-6 mediated its interaction with SYP-1. **(H)** The N terminus of SYP-6 interacted with SYP-3. **(I)** The yeast two-hybrid system was used to assess the self-interaction of the central coiled-coil regions of three SYP proteins (SYP-1-CC, SYP-5-CC, and SYP-6-CC) fused to the AD and DB of Gal4. +, fused constructs; –, empty vectors. SYP-1-CC exhibited self-interaction. SYP-5-CC (DB) and SYP-6-CC (DB) exhibited strong self-activation, and their self-interactions were not assessable by this system. **(J and K)** Self-interactions of SYP-5-CC and SYP-6-CC were detected by IP and immunoblot analysis as performed in B–H. **(L)** Schematic diagram of protein interaction network between SC components. SYP-5 and SYP-6 belong to distinct SC assembly units. Cylinders represent α-helix core of the SYPs. The copy number and orientation of each SYP protein in a unit may require further determination.

liquid crystalline property to the SC. Isolated charge blocks among linear protein sequences are known as CIEs (Pak et al., 2016). SC sequence scanning revealed that negative CIEs are more frequently present within IDRs of SYPs (Fig. 8, A–C), especially in SYP-4, SYP-5, and SYP-6. Analysis of the germline proteome indicate that the presence of CIEs is not a general feature of IDRs since only 30.4% of the IDR segments contain a negative CIE and 24.9% of IDRs contain a positive CIE. Long-range CIEs (>20 aa) that are present in SYP-4, SYP-5, and SYP-6 were found only in 8.7% and 5.2% of the IDRs for negative and positive CIEs, respectively (Fig. 8 C). Gene ontology analysis revealed that CIE-containing proteins are highly enriched in chromosome-related biological processes, suggesting that CIEs may play important roles in controlling chromosome dynamics, consistent with their potential roles in SC regulation (Fig. S5 A). Interestingly, CIEs are also enriched in the C-terminal tails of SC TF proteins and SC client proteins or SC regulators across organisms (Fig. S5, B–D), underscoring the importance of CIEs in SC-related activities.

C-terminal charged IDR of SYP-5 is essential for SC regulation

To determine the roles of IDRs in SC regulation, we generated a *syp-5(delC)* mutant that expressed SYP-5 lacking the C-terminal charged tail (Fig. S2 and Fig. 8 D). Importantly, *syp-5(delC)* mutants showed a similar phenotype to the *syp-5* null mutants with high rates of Emb (20.2%) and Him (9.2%; Fig. 8 E). Moreover, cytological analysis revealed that chromosome synapsis, SC disassembly, and SC loading were perturbed (Fig. 8, F and G), as in the *syp-5* null mutants. Moreover, SYP-5 immunostaining in *syp-5(delC)* mutants also showed impaired SYP-5 chromosome loading, further supporting the role of C-terminal IDR in SC regulation (Fig. S4 B).

Interestingly, replacing SYP-5 C-terminal IDR with SYP-6 C-terminal IDR in *syp-5(syp-6 C)* mutants also perturbed chromosome synapsis and normal disassembly of the SC (Fig. S2, Fig. 6 D, and Fig. 8 H). While the SC was enriched toward one end of the chromosomes and formed bright stretches upon pachytene exit in the wild-type background, the SC formed only small foci in *syp-5(syp-6 C)* mutants at the corresponding stage. However, during the pachytene stage, SC loading was slightly elevated in *syp-5(syp-6 C)* mutants, although synapsis defects were observed (Fig. 8 I). The perturbed chromosome synapsis and SC disassembly kinetics in *syp-5(syp-6 C)* mutants further suggests the involvement of C-terminal IDRs of SYP-5 and SYP-6 in SC regulation.

Analysis of GFP::COSA-1 focus formation in late pachytene nuclei of *syp-5(delC)* and *syp-5(syp-6 C)* mutants showed normal CO control in both mutants (Fig. 8, J–L), suggesting defects in SC disassembly are not an indirect consequence of the loss of CO control.

CIEs are essential for SC regulation

To explore the role of CIEs in SC formation, a subset of the negatively charged amino acids within the CIEs in the IDRs of SYP-5 and SYP-4 were replaced with lysines in *syp-5(14K)* mutants and *syp-4(22K)* mutants (Fig. 9 A and Fig. S2). The clustered CIEs were eliminated in these mutants without affecting protein secondary structures (Fig. 9 A). Both mutants showed Emb (6.5% in *syp-5(14k)* and 63.4% in *syp-4(22K)*) and Him (3% in *syp-5(14k)* and 28.9% in *syp-4(22K)*) phenotypes (Fig. 9 B). Synapsis defects were also observed in these mutants in the region corresponding to the mid-pachytene in wild type (Fig. 9 C). Compared with *syp-5(14K)* mutants, mutations in *syp-4* resulted in more severe synapsis defects, where highly fragmented SC was observed. Moreover, premature SC disassembly was also observed in both mutants (Fig. 9 C). Quantification of SYP-2::GFP intensities also revealed significantly impaired SC loading in these mutant backgrounds, with a more severe impact observed in *syp-4(22K)* mutants (Fig. 9 D). Consistently, chromosome association of mutated SYP-5 was also reduced in *syp-5(22K)* mutants (Fig. S4 B). These observations highlight the role of the CIEs in SC regulation.

Analysis of the CO designation marker showed increased GFP::COSA-1 foci in both *syp-5(14K)* and *syp-4(22K)* mutant backgrounds (Fig. 7, E–G), suggesting an abnormal CO control, which may in turn contribute to defects in SC disassembly. During late diakinesis, while the majority of nuclei contained six DAPI-stained bodies in *syp-5(14K)* mutants, more than six DAPI-stained bodies were frequently observed in *syp-4(22K)* mutants (Fig. 9, H and I), suggesting that the additional GFP::COSA-1 foci in these mutants were abnormally designated CO sites that could not be efficiently converted to stable interhomologue connections in *syp-4(22K)* mutants. These analyses thus indicated the critical roles of CIEs in SC regulation and CO control.

The phase separation property may underlie SC asymmetric localization upon pachytene exit

SIM analysis of SC central region components revealed their gradual concentration toward one end of each chromosome upon pachytene exit (Fig. 10, A–C), resembling a phase separation process to reduce its surface tension. The phase separation property of SYP-5 may contribute to this asymmetric localization. Consistent with SC disassembly defects observed in *syp-5(delC)* and *syp-5(14K)* mutants, C-terminal–truncated or CIE mutated SYP-5 also showed impaired phase separation properties in cells, although they were still able to form aggregates (Fig. 10, D–E). Interestingly, although SC disassembly defects were observed in *syp-5(syp-6 C)* mutants, C terminus–replaced SYP-5 did not show an impaired phase separation property, which is consistent with the unimpaired SC loading in *syp-5*

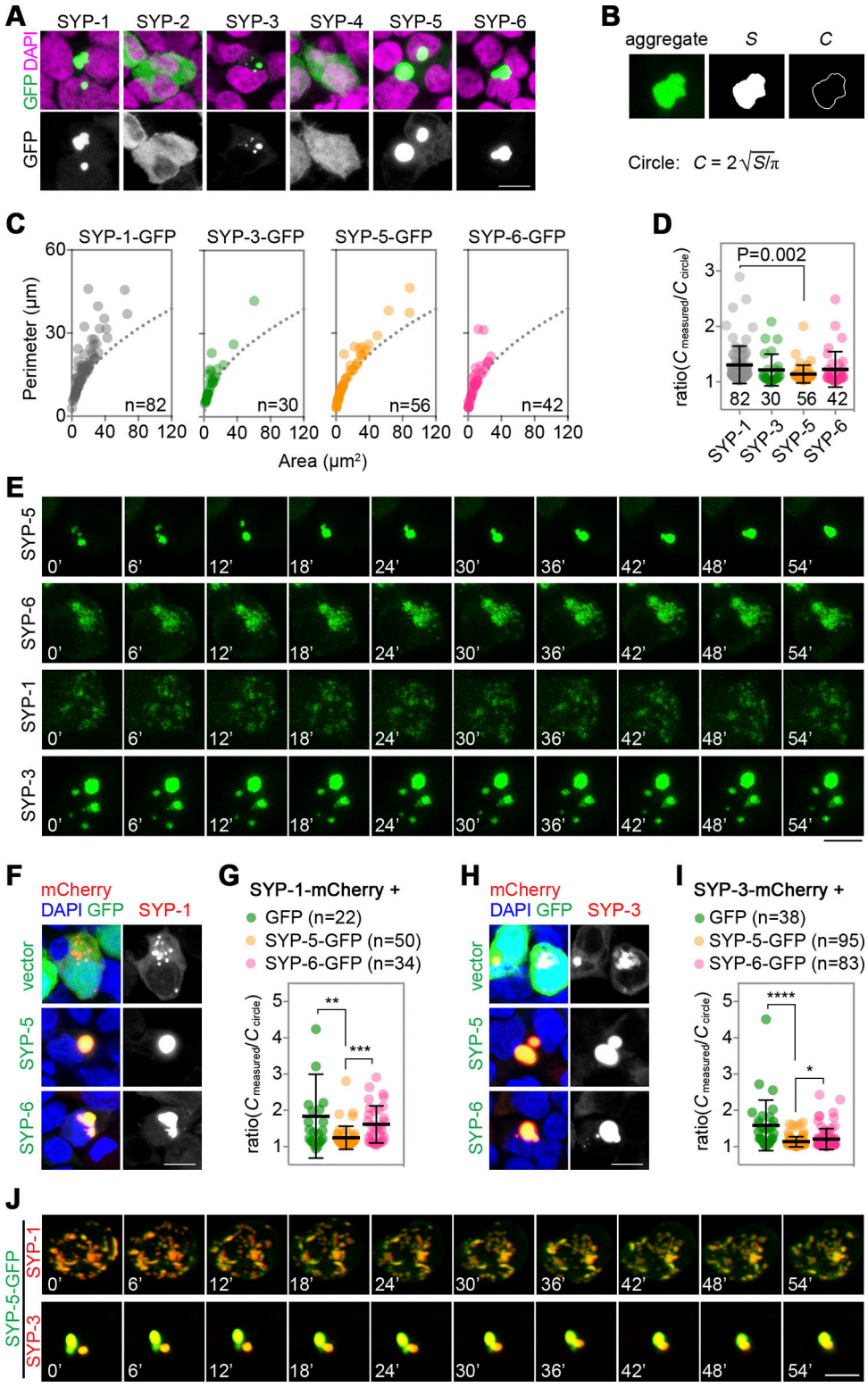

Figure 7. **Analysis of phase separation properties of SYP proteins in cells. (A)** Expression of GFP-tagged SYPs (green) in 293T cells. Nuclear DNA was stained with DAPI (magenta). Bar, 5 µm. **(B)** Evaluation of phase separation properties of proteins by measuring aggregate areas (*S*) and their perimeters (*C*) in the cells. **(C)** Area and perimeter plots of SYP aggregates measured as in B. Gray dotted curves represent the area and perimeter of the circle. **(D)** Plots show the ratio of $C_{measured}$ versus C_{circle} of the indicated SYP proteins. Bars represent the mean ± SD of the ratio, and numbers of cells measured are indicated. Two-tailed unpaired *t* test was performed for statistical analysis. **(E)** Live cell tracking of GFP-tagged SYPs in 293T cells. Fusion of SYP-5 aggregates was observed. Bar, 10 µm. **(F)** Coexpression of SYP-1-mCherry (red) and indicated GFP-tagged proteins (green). Nuclear DNA was stained with DAPI (blue). Bar, 5 µm. **(G)** Perimeter analysis of coexpressed SYP-1 aggregates in F. Bars represent the mean ± SD of the ratio, and numbers of cells measured are indicated. **, P = 0.0015; ***, P = 0.00015 (two-tailed unpaired *t* test). **(H)** Coexpression of SYP-3-mCherry (red) and indicated GFP-tagged proteins (green). Nuclear DNA was

stained with DAPI (blue). Bar, 5 µm. **(I)** Perimeter analysis of coexpressed SYP-3 aggregates in H. Bars represent the mean ± SD of the ratio, and numbers of cells measured are indicated. *, P = 0.039; ****, P < 10^{-7} (two-tailed unpaired *t* test). **(J)** Live cell tracking of SYP-5-GFP (green) coexpressed with SYP-1-mCherry or SYP-3-mCherry (red) in 293T cells. Fusion of SYP-5/SYP-3 aggregates was observed. Bar, 10 µm. Areas of yellow indicate colocalization of the co-expressed proteins in F, H, and J.

(syp-6 C) mutants (Fig. 8 I). Since chromosome association of SYP-6 is lost at the late pachytene stage, we speculate that the C terminus of SYP-6 may regulate its chromosome association, thus causing the premature SC disassembly in *syp-5(syp-6 C)* mutants. Nonetheless, these observations suggested the requirement of SC phase separation property in the establishment of asymmetric SC localization and subsequent bivalent remodeling.

Discussion

Mechanisms of SC assembly by phase separation

The highly dynamic nature of the SC suggests that its subunits are not stably connected and instead engage in weak interactions that allow its components to more easily associate and dissociate. This is contrary to the model that the SC is assembled through stable internal interactions and forms a filamentous structure, which is supported by the detection of stable interactions between SC components and observations of linear or branched filament-like structures formed by SC components in ectopically expressed cells or in vitro systems (Costa et al., 2005; Davies et al., 2012; Yuan et al., 1998). SC formation in meiotic cells is tightly controlled both temporally and spatially, and the complex is only assembled into a linear structure between paired homologous chromosomes once the meiotic chromosome axes are formed. Thus, the filamentous structure formed by ectopically expressed SC components may reflect an aberrant configuration that occurs in the absence of a normal regulatory/binding partner. In this study, we provide evidence that SC components form assembly units through interactions between their coiled-coil domains and propose that these units then weakly interact to form the SC. This explains the apparent discrepancy between the stable interactions of SC components and the dynamic nature of the SC.

Our work also highlights the role of IDRs in SC assembly. IDRs within the SC proteins contain abundant CIEs that we suggest are involved in multivalent weak interactions between SC assembly units, conferring the SC with a liquid crystalline property. Notably, negative CIEs are more abundant than positive ones among SC components. The mechanism by which negative CIEs induce SC phase separation is suggested by a previous report that phase separation of a negatively charged intrinsically disordered protein, the Nephrin intracellular domain, is driven by coassembly with positively charged partners (counterions; Pak et al., 2016). It is possible that positively charged counterions, e.g., free soluble histones, which are abundant in cells and contain positive charges, might be involved in SC phase separation. Among the SYPs, SYP-4 has the largest IDR and most abundant CIEs, and CIE removal in SYP-4 causes severe synapsis defects in vivo. However, SYP-4 on its own does not form aggregates or phase-separate in 293T cells. The molecular mechanism for how SYP-4 contributes to SC formation and SC phase separation warrants further investigation.

Although the presence of CIEs in SC proteins reveals a driving force for SC assembly by phase separation, other types of interactions also likely exist. We previously reported that N-terminal acetylation of SYP-1 is essential for SC assembly, and this may involve hydrophobic interactions (Gao et al., 2016). Indeed, the requirement for hydrophobic interactions in SC assembly has been suggested by another study (Rog et al., 2017). These various types of interactions are orchestrated to form multivalent weak cooperative interactions that can provide interaction specificities and dynamic properties. The presence and abundance of different types of interacting elements within the SC components may define SC dynamic property in an organism. Additional in vivo and in vitro studies are required to determine these specific requirements and how they are orchestrated for SC formation.

Conservation of CIE-mediated SC regulation across organisms

The involvement of CIEs in SC formation and regulation may be conserved across organisms. Although TF proteins from different organisms show no sequence similarity, the presence of both types of CIEs at the C termini of the TFs is highly conserved (Fig. S5 B). In fact, SC assembly is abolished in a yeast mutant with removal of a negative CIE from the TF C terminus by a ZIP1 in-frame deletion (Fig. S5 B; Tung and Roeder, 1998), underscoring the importance of CIEs in the TF C terminus. In yeast, poly-SUMOylation of the central element protein Ecm11 is essential for SC assembly (Humphryes et al., 2013; Leung et al., 2015). Interestingly, SUMO also has a C-terminal negative CIE (data not shown), and polySUMO chains thus create negative CIEs for Ecm11. These findings suggest that the abundance of negative CIEs in SC central elements may be widely involved in SC assembly and/or regulation across organisms.

Protein compartmentalization within the SC

The SC may represent a novel type of phase separation–driven linear structure between homologous chromosomes. Super-resolution microscopy data suggest that the SC forms double layers in the nematode, fly, and mouse (Cahoon et al., 2017; Schücker et al., 2015; Woglar and Villeneuve, 2018). This structure differs significantly from the canonical phase-separated droplet-like structures. Upon pachytene exit, specific enrichment of SC components toward one end of the chromosomes resembles a phase separation process to reduce surface tension. As in the case of other membraneless organelles, the SC provides a unique stage for compartmentalized cellular activities. Many recombination-related factors and kinases that act during meiosis, e.g., BRC-1/2, ZHP-1/2/3/4, and polo-like kinase 2, are recruited to the SC during early meiotic prophase (Bhalla et al., 2008; Harper et al., 2011; Janisiw et al.,

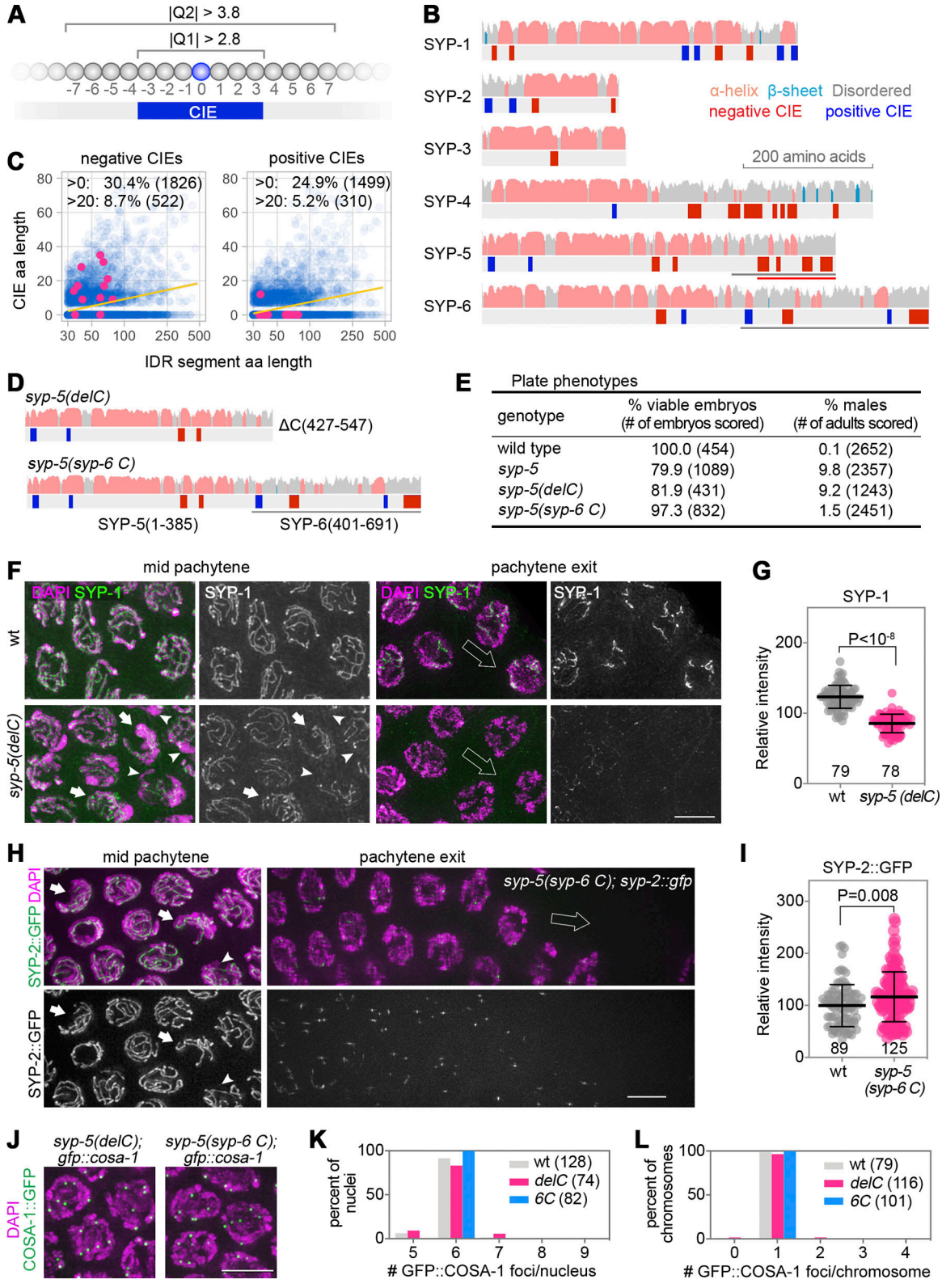

Figure 8. **SC components are enriched in CIEs. (A)** Criteria for CIE identification. Q1 and Q2 represent the net charges of amino acids in the indicated regions. **(B)** CIE distribution among *C. elegans* SC components. Secondary structures of SYP proteins are shown at the top, and CIE blocks are shown at the bottom (red, negative CIE; blue, positive CIE). The red horizontal line in B indicates the region deleted in the *syp-5(delC)* mutants, and gray horizontal lines indicate the regions used for replacement in *syp-5(syp-6 C)* mutants. **(C)** CIE distribution in the *C. elegans* germline proteome. Percentages and numbers of the IDRs that contain CIEs (or long-range CIEs >20 aa) are indicated. IDR segments of the germline proteome are shown in blue, and IDR segments of SC components are highlighted in red. Yellow lines depict smoothed conditional means of CIE lengths. **(D)** Schematic diagrams of SYP-5 protein products in *syp-5(delC)* and *syp-5(syp-6 C)* mutants. The gray horizontal line indicates the replaced C terminal region in *syp-5(syp-6 C)* mutants. **(E)** Plate phenotype analysis for

syp-5(delC) and *syp-5(syp-6 C)* mutants. **(F)** Immunostaining for SYP-1 (green) in gonads dissected from indicated genotypes. Chromatin was stained with DAPI (magenta). Chromosomes lacking SYP-1 signal (white arrowheads) and nuclei with crescent-shaped chromosome organization (arrows) are indicated. Bar, 5 µm. **(G)** Quantification of SYP-1 loading in mid-pachytene nuclei of the indicated genotypes. Bars represent the mean ± SD of normalized SYP-1 fluorescent intensities. Numbers of nuclei measured are indicated, and two-tailed unpaired *t* test was performed for statistical analysis. **(H)** Examining SYP-2::GFP (green) localization in *syp-5(syp-6 C)* mutants showed defects in synapsis and SC disassembly. Chromatin was stained with DAPI (magenta). Chromosomes lacking SYP-2::GFP signal (arrowheads) and nuclei with crescent-shaped chromosome organization (arrows) are indicated. Bar, 5 µm. **(I)** Quantification of SYP-2::GFP loading in mid-pachytene nuclei of the indicated genotypes. Bars represent the mean ± SD of normalized SYP-2::GFP fluorescent intensities. Numbers of nuclei measured are indicated, and two-tailed unpaired *t* test was performed for statistical analysis. **(J)** Formation of GFP::COSA-1 foci (green) in late pachytene nuclei from indicated genotypes. Chromatin was stained with DAPI (magenta). Bar, 5 µm. **(K and L)** Quantification of GFP::COSA-1 foci in the indicated genotypes. Numbers of nuclei and chromosomes scored are indicated. wt, wild type.

2018; Li et al., 2018; Zhang et al., 2018). Interestingly, these proteins usually contain a high proportion of IDRs (39%–83% of their sequences) and both types of CIEs (Fig. S5 D). The *Drosophila* protein Sororin is also recruited to the SC (Gómez et al., 2016) and contains a high proportion of IDRs (83.4%) and numerous CIEs (18 CIEs; Fig. S5 D). The SC compartmentalization of these factors may be regulated by posttranslational modification of the SC and/or of the factors themselves. The prevalence of IDRs and CIEs among SC components, regulators, and clients suggests a unifying regulatory mechanism for SC-related activities.

Role of the SC in axis remodeling

Our data support a model in which SC components assemble into the SC structure through phase separation, and we showed that localization and retention of SC proteins on the short arms in late prophase is required for subsequent proper chromosome remodeling and accurate meiotic segregation. Association of the SC proteins on the short arm of the bivalent may alter the binding preference of some axis-associated factors, leading to axis remodeling. We propose that remodeling defects in *syp-5* mutants result in the loss of predefined bivalent segregation pattern. However, examining the localization of kinetochore factors and tracking the chromosome segregation process during meiosis will help clarify the specific segregation errors. The function of the SC proteins in mediating axis remodeling may also exist in other organisms. In mammals, flies, and yeast, SC central region components are preferentially retained at centromeres and pericrossover regions and are lost from the rest of the chromosome arms during late meiotic prophase (Bisig et al., 2012; Gladstone et al., 2009; Newnham et al., 2010; Qiao et al., 2012; Takeo et al., 2011). Prolonged association of the SC proteins in chromosome subdomains could also result in remodeling of the meiotic axis in these organisms, which is a possibility that warrants further investigation.

Materials and methods

C. elegans strains and culture conditions

Bristol N2 was used as the wild-type strain in this study, and all mutants were derived from the N2 background. Worms were cultured at 20°C on nematode growth media agar plates spread with *Escherichia coli* OP50 according to the standard method (Stiernagle, 2006). CRISPR-Cas9 genomic editing was used to create *syp-4*, *syp-5*, and *syp-6* mutants and *syp-5*, *syp-6* C-terminal GFP-tagged lines. Briefly, young adult N2 hermaphrodites were injected with a set of plasmids expressing Cas9 (*Peft-3*Cas9-SV40 NLS*tbb-2* 3′UTR, 200 ng/µl), the targeting single guide RNA (100 ng/µl), and mCherry coinjection markers (pCFJ90, 5 ng/µl; pCFJ104, 5 ng/µl). Plasmids containing a donor template sequence were coinjected (100 ng/µl) when precise genome editing was desired. F1 progeny expressing mCherry coinjection marker was singled and screened for successful genome edits via PCR and sequencing. A summary of these gene alterations is shown in Fig. S2. Primer sequences for PCR screen are as follow (amplicon size in parentheses): syp-5(cac1)F: 5′-CCGTGCGCC TTTAATTTTTA-3; syp-5(cac1)R: 5′-TTTTTGTCGCTGATTGAT GC-3′ (454 bp); syp-5(cac4)F: 5′-TCGTTTCGGTAATTTCTGGC-3; syp-5(cac4)R: 5′-AGGAAAACGTCGAAACTAGG-3′ (1,560 bp); syp-5(cac27)F: 5′-CCAGAGCGGTCCGTAAATC-3; syp-5(cac27)R: 5′-GTTCGAGAGAGACGCACAATA-3′ (1,317 bp); syp-5(cac34)F: 5′-ATAAGTTCGACTACACCACC-3; syp-5(cac34)R: 5′-ATGTGA CAAATCATGTTTCA-3′ (2,518 bp); syp-5(cac43)F1: 5′-GGCGAT TTTTCTAGATGGATAAGT-3; syp-5(cac43)R2: 5′-AGTGAAATA CGTAGAATACCTCA-3′ (707 bp); syp-5(cac43)F2: 5′-AAACGA AGAATTGGTCATCA-3; syp-5(cac43)R2: 5′-CGTCGAAACTAG GAAGAAAGC-3′ (944 bp); syp-6(cac3)F: 5′-AATGTCGTTGAG AGGCTTCC-3; syp-6(cac3)R: 5′-GTTTTAGTCGTCACCATCCC-3′ (917 bp); syp-6(cac5)F: 5′-ATGGCGGTCTAGATCAAACG-3; syp-6(cac5)R: 5′-GCACGAAAAATGATGCAAAA-3′ (1,457 bp); syp-4(cac42)F: 5′-AAGAGACGAACACCGAGGCT-3; and syp-4(cac42) R: 5′-CGCCCGCTCCAGAAGTTGCT-3′ (1,627 bp).

C. elegans strains used in this study

The following strains were used: AV630: *meis8 [pie-1p::gfp::cosa-1 + unc-119(+)] II*; JH2749: *unc-119(ed3) III; axIs1914[syp-3p::GFP::syp-3 3′UTR + unc-119(+)]*; MGC2: *syp-5(cac1) I*; MGC4: *syp-5(cac1) I; meis8 [pie-1p::gfp::cosa-1 + unc-119(+)] II*; MGC5: *syp-5(cac1) I; wgIs227[syp-2::TY1::EGFP::3xFLAG(92C12) + unc-119(+)]*; MGC10: *syp-5(cac1) I; ojIs50[pie-1p::GFP::air-2 + unc-119(+)]*; MGC13: *syp-6(cac3) I; MGC14: syp-5::gfp(cac4) I*; MGC18: *syp-6::gfp(cac5) I*; MGC46: *syp-5(cac1) syp-6(cac3) I*; MGC65: *syp-6(cac3) I; meis8 [pie-1p::gfp::cosa-1 + unc-119(+)] II*; MGC66: *syp-6(cac3) I; wgIs227[syp-2::TY1::EGFP::3xFLAG(92C12) + unc-119(+)]*; MGC70: *syp-5::gfp(cac4) I; syp-1(me17) V/nT1[unc-?(n754)let-?] (IV;V)*; MGC86: *syp-5(delC) (cac27) I*; MGC98: *syp-5(syp-6 C)(cac34) I*; MGC114: *syp-5(cac34) I; meis8 [pie-1p::gfp::cosa-1 + unc-119(+)] II*; MGC137: *syp-5(cac34) I; wgIs227[syp-2::TY1::EGFP::3xFLAG(92C12) + unc-119(+)]*; MGC126: *syp-4(cac42) I*; MGC128: *syp-5(cac43) I*; MGC152: *syp-5(cac43) I; wgIs227[syp-2::TY1::EGFP::3xFLAG(92C12) + unc-119(+)]*; MGC155: *syp-4(cac42) I; meis8 [pie-1p::gfp::cosa-1 + unc-119(+)] II*; MGC156: *syp-4(cac42) I; wgIs227[syp-2::TY1::EGFP::3xFLAG(92C12) + unc-119(+)]*; MGC181: *syp-5(cac43) I; meis8 [pie-1p::gfp::cosa-1 + unc-119(+)] II;*

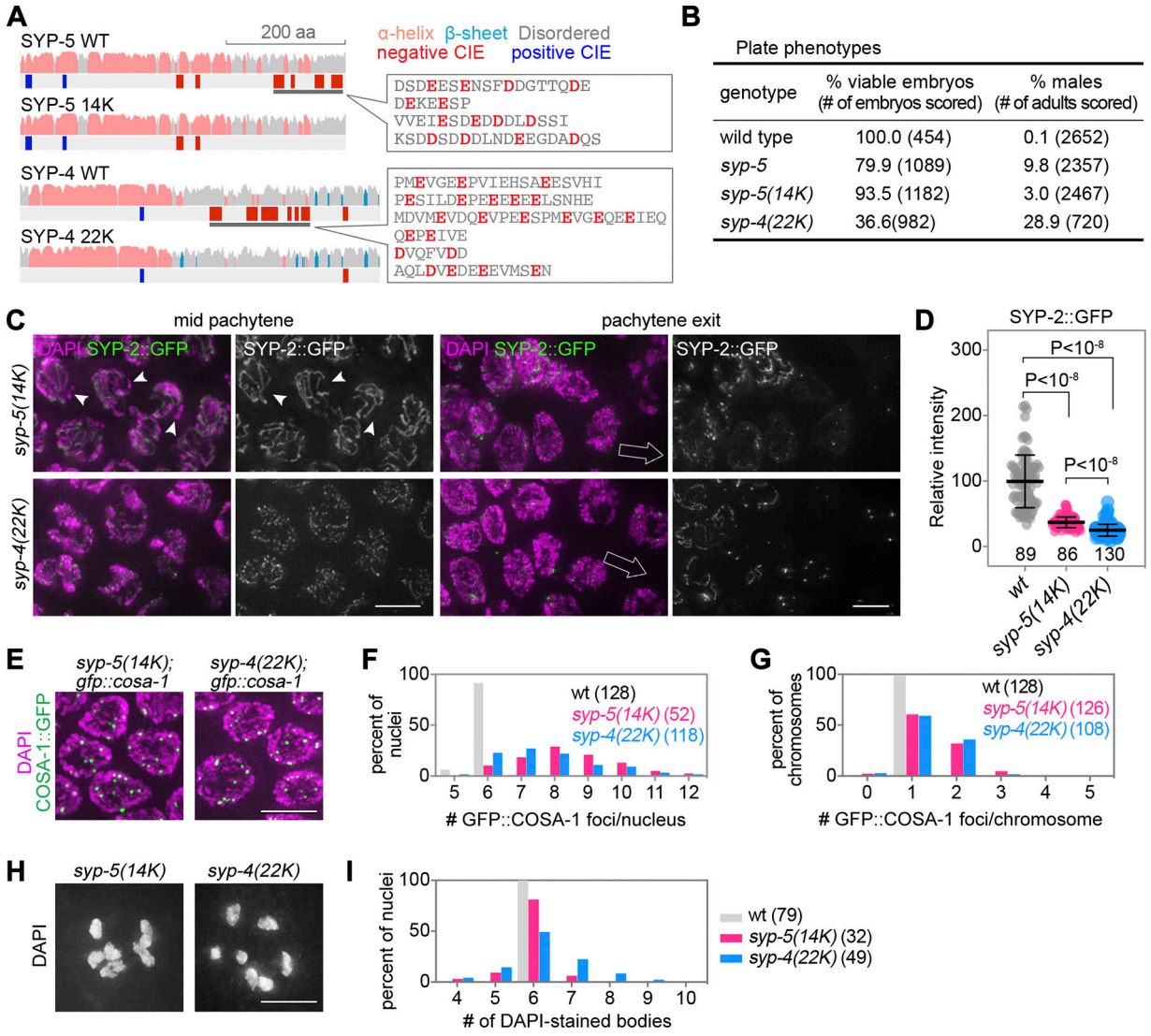

Figure 9. **CIEs are involved in SC regulation. (A)** Schematic diagrams of wild-type or CIE-removed SYP-5 and SYP-4 proteins. Secondary structures of SYP proteins are shown at the top, and CIE blocks are shown at the bottom (red, negative CIE; blue, positive CIE). The C-terminal CIEs were removed by mutating a group of aspartic acids or glutamic acids to lysines within the indicated gray horizontal lines (mutated amino acids are highlighted in red). **(B)** Plate phenotype analysis of *syp-5(14K)* and *syp-4(22K)* point mutants. **(C)** *syp-5(14K)* and *syp-4(22K)* point mutants showed defects in SC formation and disassembly during meiotic prophase. Arrowheads indicate chromosomes without the SC. Open arrows indicate orientation of meiotic progression from late pachytene into diplotene. Chromatin was stained with DAPI (magenta). Bar, 5 µm. **(D)** Quantification of SYP-2::GFP loading in mid-pachytene nuclei of the indicated genotypes. Bars represent the mean ± SD of normalized SYP-2::GFP fluorescent intensities. Numbers of nuclei measured are indicated, and two-tailed unpaired *t* test was performed for statistical analysis. **(E)** Formation of GFP::COSA-1 foci (green) in late-pachytene nuclei from indicated genotypes. Chromatin was stained with DAPI (magenta). Bar, 5 µm. **(F and G)** Quantification of GFP::COSA-1 foci in the indicated genotypes. **(H and I)** Quantification of DAPI-stained bodies at diakinesis in the indicated genotypes. Bar, 5 µm. wt, wild type.

OP227: *unc-119(ed3) III; wgIs227[syp-2::TY1::EGFP::3xFLAG(92C12) + unc-119(+)]*; and WH371: *unc-119(ed3) III; ojIs50[pie-1p::GFP::air-2 + unc-119(+)]*.

Antibodies used in this study

The following primary antibodies were used at the indicated dilutions: goat anti–SYP-1 antibody (1:1,000 for immunofluorescence [IF] staining; MacQueen et al., 2002), rabbit anti–SYP-5 (1:1,000 for IF), mouse anti-HA (1:2,000 for Western blot; Sigma-Aldrich), chicken anti-GFP (1:2,000 for Western blot; Abcam), rabbit anti–phospho-H3 (Ser10; 1:1,000 for IF; Fisher Scientific), guinea pig anti–HTP-3 (1:500 for IF; Goodyer et al., 2008). HRP-conjugated anti-mouse (1:5,000; Cell Signaling), HRP-conjugated anti-chicken (1:5,000; Proteintech), anti–goat-Alexa488 (1:200; Jackson ImmunoResearch Laboratories), and anti–rabbit-Cy3 (1:200; Jackson ImmunoResearch Laboratories). SYP-5 ploYclonal antibody was generated in this study, and the antigen used for antibody production is illustrated in Fig. S4 A.

IP and MS analyses

IP of GFP-tagged SYP proteins was performed with nuclear extracts. Synchronized young adult worms were shredded by

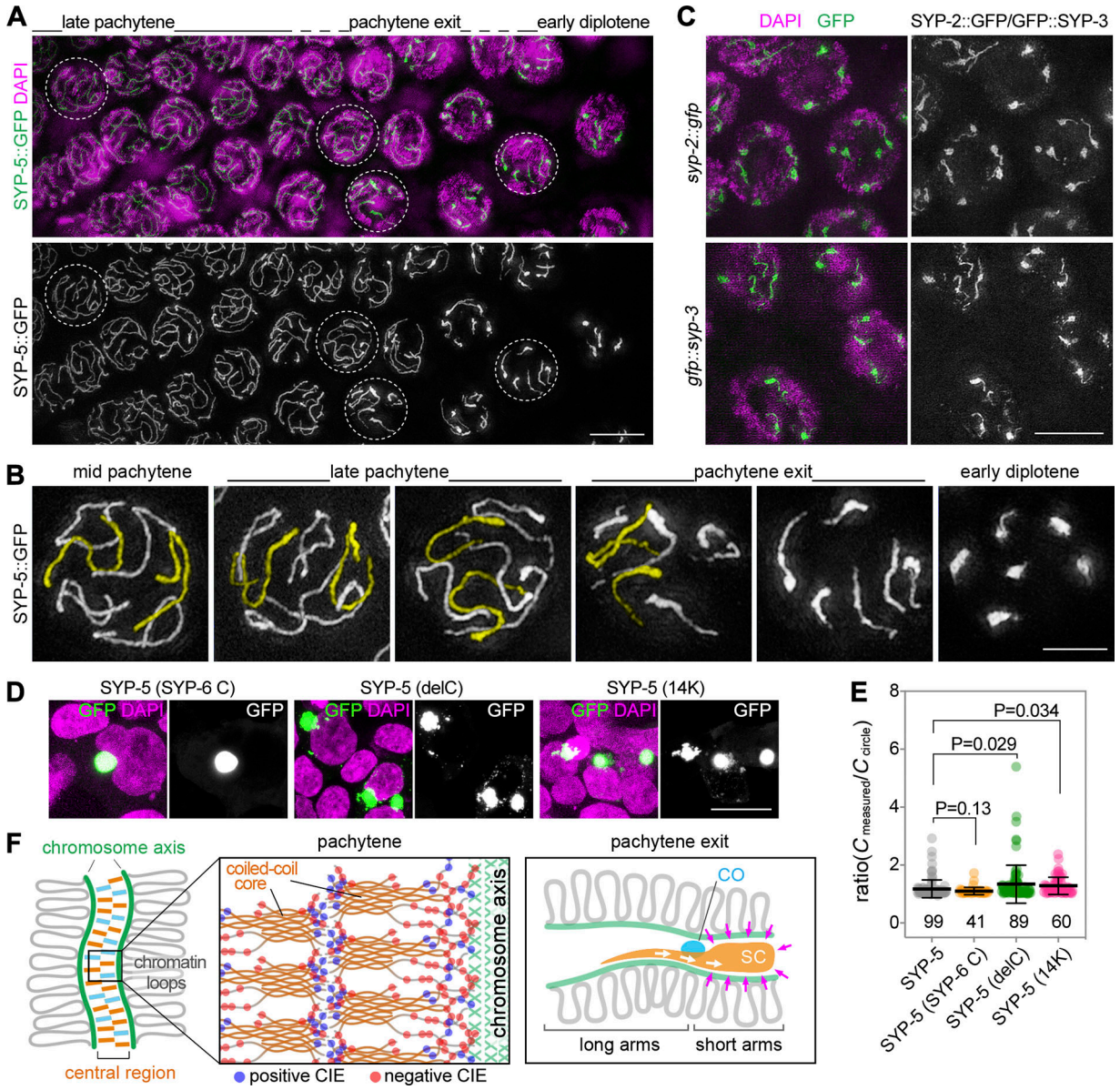

Figure 10. **Phase separation property of the SC may underlie its asymmetric localization during pachytene exit. (A)** SIM analysis of SYP-5::GFP (green) localization on chromosomes during late pachytene to diplotene transition. Chromatin was stained with DAPI (magenta). Magnified images for circled nuclei are shown in B. Bar, 5 µm. **(B)** SYP-5::GFP started to accumulate toward one end of the chromosomes from late pachytene stage. A subset of the SC tracks was pseudocolored in yellow for ease of identification. Bar, 2 µm. **(C)** SIM analysis of SYP-2::GFP and GFP::SYP-3 (green) localization on chromosomes during late pachytene to diplotene transition. Chromatin was stained with DAPI (magenta). Bar, 5 µm. **(D)** Expression of mutated SYP-5 fused with GFP (green) in 293T cells. Nuclear DNA was stained with DAPI (magenta). Bar, 10 µm. **(E)** Phase separation property analysis of mutated SYP-5. Bars represent the mean ± SD of the ratio. Numbers of cells measured are indicated, and two-tailed unpaired *t* test was performed for statistical analysis. **(F)** Model for SC assembly and asymmetric SC localization in *C. elegans*. SYPs form assembly units through coiled-coil–mediated stable interactions. The IDRs of SC components extending from the coiled-coil cores (orange) are critical for interactions between the units and drive SC formation. CIEs (blue and red dots) and other putative interaction elements (not illustrated) within the IDRs confer multivalency to the assembly units and help define SC dynamic property. During pachytene exit, the SC fluid gradually accumulates toward the short chromosome arms separated by the CO "dam" (cyan), representing a phase separation structure that tends to reduce surface tension (magenta arrows). White arrows indicate the fluid direction.

vortexing in 15-ml conical tubes containing small sharp broken glass coverslips in ice-cold nuclear isolation buffer (10 mM Hepes at pH 7.6, 1 mM EGTA, 1.5 mM $MgCl_2$, 10 mM KCl, 250 mM sucrose, 0.5 mM DTT, and protease inhibitor mixture; Roche). Worm debris was removed by two rounds of centrifugation at 30*g* for 5 min, and nuclei in the supernatants were collected by centrifugation at 800*g* for 10 min. Nuclei were washed twice with the nuclear isolation buffer followed by additional centrifugation. Isolated nuclei were suspended with lysis buffer (50 mM Hepes at pH 7.4; 1 mM EGTA; 3 mM $MgCl_2$; 300 mM KCl; 10% glycerol; 1% NP-40; 1 mM DTT; and protease inhibitor mixture) and incubated on ice for 10 min. Insoluble components in the nuclear extracts were removed by centrifugation at 16,000*g* for 5 min. Nuclear extracts were incubated

with GFP-Trap agarose beads (ChromoTek) for 4 h at 4°C. Immunoprecipitated proteins were eluted by boiling in 2% SDS in 20 mM Tris (pH 7.4) for 5 min. Eluted proteins were precipitated with the ProteoExtract Protein Precipitation Kit (Calbiochem) and digested with trypsin for MS analysis. To identify SYP-binding partners, the SYP IP data were compared with data from at least three unrelated IPs that were performed in an identical manner but targeted different GFP-tagged proteins. Proteins detected in SYP immunoprecipitates of two biological replicates were considered specific binding partners.

Immunofluorescence microscopy

Gonads were dissected from young adult worms (24 h after L4) in dissection buffer (25 mM Hepes at pH 7.4, 118 mM NaCl, 48 mM KCl, 2 mM EDTA, 5 mM EGTA, 0.1% Tween-20, and 10 mM NaN_3) on polylysine glass slides, which were then freeze-cracked on dry ice. Slides were fixed in methanol (−20°C) for 1 min and in 4% paraformaldehyde in PBS at RT for 25 min. Slides were blocked with 0.5% BSA in PBST (1× PBS, 0.1% Tween-20) for 1 h at RT before the incubation with primary antibodies overnight at 4°C. After three washes in PBST, slides were incubated with appropriate secondary antibodies at RT for 2 h followed by an additional three washes in PBST. DAPI (1 µg/ml; Sigma-Aldrich) was used to stain DNA, and the gonads were mounted with Vectashield (Vector Laboratories) and #1.5 glass coverslips (VWR). Fluorescence microscope images, except those shown in Fig. 4 E and Fig. S3 D, are maximum-intensity projections through 3D data stacks of whole nuclei. Wide-field images were captured through whole nuclei at 200-nm intervals on a DeltaVision OMX microscope system with 60×/1.42 and 100×/1.40 objective lenses by SoftWoRx software (Applied Precision) in the conventional imaging mode. Images were deconvolved using a conservative algorithm with 10 iterations. Structure illumination microscopy images were captured as 125 nm–spaced Z stacks on the DeltaVision OMX microscope system with 60×/1.42 lens in 3D-SIM mode; 3D-image reconstruction and registration were performed with SoftWoRx. To obtain optimal images of gonads, immersion oil with a refractive index of 1.522 was used. Fluorescence microscope images shown in Fig. 4 E and Fig. S3 D were captured on a LEICA DM6 B microscope with 40× lens by LAS X software.

SC intensity analysis

To analyze SC loading by measuring fluorescence intensity of SC components, Z stacks of whole germ cell nuclei were acquired at 200-nm intervals with fixed parameters for the different genotypes. Maximum-intensity projection of 3D data stacks of the whole nuclear signal was first generated with SoftWoRx software, and additive fluorescent signal for each nucleus was measured using a combination of tools in ImageJ (National Institutes of Health) and an in-house R script. Specifically, 2D image data for each nucleus were selected and exported as "Text image" with ImageJ. The obtained text files were batch processed with R script to measure the background signal intensities and to calculate additive fluorescent signal above the background for each nucleus. Additive signal intensity for each nucleus was normalized to the local background signal before being used for comparison. R script used for the calculation is available upon request.

In vitro mapping of interactions between SC components

Coding sequences of SYP proteins and their truncated forms were cloned into mammalian expression plasmids with a cytomegalovirus promoter and fused with a GFP or GST-HA tag. Plasmids were cotransfected into 293T cells that were cultured in Dulbecco's modified Eagle's medium supplemented with 10% fetal calf serum at 37°C in a humidified atmosphere with 5% CO_2. Polyethylenimine reagent (Sigma-Aldrich) was used for plasmid transfection. Cells were lysed after 24 h in cell lysis buffer composed of 50 mM Hepes at pH 7.4, 1 mM EGTA, 3 mM $MgCl_2$, 300 mM KCl, 10% glycerol, 1% Nonidet P-40, 1 mM DTT, and protease inhibitor mixture. Interactions between cotransfected proteins were examined by IP and Western blot analysis. GFP-Trap magnetic beads (ChromoTek) or anti-HA agarose beads (Sigma-Aldrich) were used to perform IP.

Yeast two-hybrid analysis

cDNA of the central coiled coils of SYP-1, SYP-5, and SYP-6 were cloned into the 2-µ Gateway destination vectors pVV213 (activation domain [AD], *LEU2*+) and pVV212 (Gal4 DNA-binding domain [DB] *TRP1*+). AD-fusions and DB-fusions were transformed into *MATa* Y8800 and *MATα* Y8930 yeast strains, respectively. *MATa* Y8800 and *MATα* Y8930 were mated on yeast extract peptone dextrose plates, and diploids carrying both plasmids were selected on synthetic complete medium lacking Leu and Trp (Leu-Trp) plates. The interactions were assessed by growth on selective plates (-Leu -Trp -Ade) at 30°C.

Phase separation trend analysis and live cell imaging

Plasmids expressing fluorescent protein-fused SYPs were transfected into 293T cells cultured on glass coverslips. 24 h after transfection, cells were fixed with 4% paraformaldehyde in PBS and stained with DAPI. Images of 3D data stacks of whole cells were captured with Dragonfly High-speed Confocal Imaging Platform (100× objective) with Fusion software and processed with Imaris Viewer (ANDOR; Oxford Instruments). Images presented in Fig. 7 were maximum-intensity projections through 3D data stacks of whole cells. Areas and perimeters of SYP protein aggregates were analyzed with the "Analyze particles" function of ImageJ software. To track SYP aggregate dynamics, cells were cultured on glass-bottom dishes (MatTek), and 20 h after transfection, culture dishes were mounted on the Dragonfly High-speed Confocal Imaging Platform with an environmental chamber supplied with 5% CO_2 at 37°C. Cells with small SYP aggregates were tracked, and images for 3D data stacks of whole cells were captured every 60 s for 1 h.

CIE scanning

To search for CIEs within proteins, amino acid sequences were scanned for charge distribution using an in-house R script and the R "Peptides" library. Parameters were set as pH = 7.0, pK_{scale} = "Lehninger." A charged block functions as a CIE when its charges are not neutralized by adjacent amino acids carrying the opposite charge. At a given amino acid position, if the net charge within a 3-aa radius was >2.8, this 7-aa region was considered

a candidate CIE; however, it was defined as a functional CIE only when its charges were not neutralized by adjacent amino acids. The criterion of a net charge >3.8 within a 7-aa radius was used to define a functional CIE. These criteria allowed us to identify CIEs that were nearly identical to those reported in a previous study (Pak et al., 2016). R script used for data analysis is available upon request.

Protein structure analysis

Protein secondary structure prediction was performed with Porter 5 (Torrisi et al., 2018 *Preprint*). For IDR segment length calculation, α-helix or β-sheep three aa or less in length were ignored and were considered part of the IDR sequence. Protein coiled-coil regions were predicted using COILS with MTIDK matrix selected (Lupas et al., 1991).

Analysis of CIE distribution in the *C. elegans* germline proteome

Protein sequences of 4606 *C. elegans* germline-expressed genes (>50 reads per kilobase per million mapped reads; from germline-specific transcriptome data of Ortiz et al. (2014) were analyzed for secondary protein structure with Porter5 (Torrisi et al., 2018 *Preprint*) and scanned for the presence of CIEs. A total of 6,015 IDR segments (at least 30 aa) were identified from 2,904 proteins. The majority of the IDR segments do not contain a CIE, and some IDRs contain multiple CIEs.

COSA-1 focus quantification

Quantification was restricted to only nuclei at the late pachytene stage, which was defined as the last 1/5 zone of a gonad region from meiotic entry to pachytene exit. Nuclei or chromosomes from at least four gonads of each genotype were analyzed. In some mutant backgrounds (e.g., *syp-5(14K)* and *syp-4(22K)* mutants), COSA-1 focus quantification was assisted by visualizing chromosome axis with HTP-3 immunostaining.

Quantification and statistical analysis

Statistical significance is reported in the figures or figure legends. Prism 7 software (GraphPad) was used to generate graphs and perform statistical analyses. Mean differences were compared with the two-tailed unpaired Student's *t* test. Data distribution was assumed to be normal, but this was not formally tested. $P < 0.05$ was considered statistically significant.

Online supplemental material

Fig. S1 shows the list of SYP-2::GFP binding proteins, translation rates, and secondary protein structure of SYPs and K09H9.1. Fig. S2 shows information for *syp* mutants created in this study. Fig. S3 shows the analysis of chromosome synapsis in *syp-5* and *syp-5 syp-6* mutants. Fig. S4 shows data for SYP-5 immunostaining in different mutant backgrounds. Fig. S5 shows enrichment analysis of CIEs in the *C. elegans* proteome and SC components across organisms.

Acknowledgments

We thank M. Zetka (McGill University, Quebec, Canada) for the HTP-3 antibody and SunyBiotech (Fuzhou, China) for assisting in creating some mutant strains.

Some strains were provided by the Caenorhabditis Genetics Center, which is funded by the National Institutes of Health Office of Research Infrastructure Programs (P40 OD010440). This work was supported by grants from the National Natural Science Foundation of China (31701176 and 31871360 to J. Gao, 31730050 to J. Zhou, 31801137 to Z. Zhang, and 31900557 to R. Wang), the National Key R&D Program of China 2017YFA0503500 (to J. Zhou), and National Institutes of Health grant R01GM072551 (to M.P. Colaiácovo).

The authors declare no competing financial interests.

Author contributions: Conceptualization, J. Gao.; methodology, J. Gao; investigation, J. Gao, Z. Zhang, S. Xie, R. Wang, S. Guo, Q. Zhao, Y. Liu, H. Nie, F. Zhang, M. Chen, L. Liu, X. Meng, M. Liu, and L. Zhao; writing – original draft, J. Gao; writing – review and editing, J. Gao, J. Zhou, and M.P. Colaiácovo; funding acquisition and resources, J. Gao, J. Zhou, and M.P. Colaiácovo; and supervision, J. Zhou and J. Gao.

Submitted: 14 October 2019
Revised: 22 January 2020
Accepted: 26 February 2020

References

Bhalla, N., D.J. Wynne, V. Jantsch, and A.F. Dernburg. 2008. ZHP-3 acts at crossovers to couple meiotic recombination with synaptonemal complex disassembly and bivalent formation in C. elegans. *PLoS Genet.* 4: e1000235. https://doi.org/10.1371/journal.pgen.1000235

Bisig, C.G., M.F. Guiraldelli, A. Kouznetsova, H. Scherthan, C. Höög, D.S. Dawson, and R.J. Pezza. 2012. Synaptonemal complex components persist at centromeres and are required for homologous centromere pairing in mouse spermatocytes. *PLoS Genet.* 8:e1002701. https://doi.org/10.1371/journal.pgen.1002701

Boeynaems, S., S. Alberti, N.L. Fawzi, T. Mittag, M. Polymenidou, F. Rousseau, J. Schymkowitz, J. Shorter, B. Wolozin, L. Van Den Bosch, et al. 2018. Protein Phase Separation: A New Phase in Cell Biology. *Trends Cell Biol.* 28:420–435. https://doi.org/10.1016/j.tcb.2018.02.004

Cahoon, C.K., and R.S. Hawley. 2016. Regulating the construction and demolition of the synaptonemal complex. *Nat. Struct. Mol. Biol.* 23: 369–377. https://doi.org/10.1038/nsmb.3208

Cahoon, C.K., Z. Yu, Y. Wang, F. Guo, J.R. Unruh, B.D. Slaughter, and R.S. Hawley. 2017. Superresolution expansion microscopy reveals the three-dimensional organization of the *Drosophila* synaptonemal complex. *Proc. Natl. Acad. Sci. USA.* 114:E6857–E6866. https://doi.org/10.1073/pnas.1705623114

Colaiácovo, M.P., A.J. MacQueen, E. Martinez-Perez, K. McDonald, A. Adamo, A. La Volpe, and A.M. Villeneuve. 2003. Synaptonemal complex assembly in C. elegans is dispensable for loading strand-exchange proteins but critical for proper completion of recombination. *Dev. Cell.* 5: 463–474. https://doi.org/10.1016/S1534-5807(03)00232-6

Costa, Y., R. Speed, R. Ollinger, M. Alsheimer, C.A. Semple, P. Gautier, K. Maratou, I. Novak, C. Höög, R. Benavente, et al. 2005. Two novel proteins recruited by synaptonemal complex protein 1 (SYCP1) are at the centre of meiosis. *J. Cell Sci.* 118:2755–2762. https://doi.org/10.1242/jcs.02402

Davies, O.R., J.D. Maman, and L. Pellegrini. 2012. Structural analysis of the human SYCE2-TEX12 complex provides molecular insights into synaptonemal complex assembly. *Open Biol.* 2:120099. https://doi.org/10.1098/rsob.120099

de Carvalho, C.E., S. Zaaijer, S. Smolikov, Y. Gu, J.M. Schumacher, and M.P. Colaiácovo. 2008. LAB-1 antagonizes the Aurora B kinase in C. elegans. *Genes Dev.* 22:2869–2885. https://doi.org/10.1101/gad.1691208

Dunce, J.M., O.M. Dunne, M. Ratcliff, C. Millán, S. Madgwick, I. Usón, and O.R. Davies. 2018. Structural basis of meiotic chromosome synapsis through SYCP1 self-assembly. *Nat. Struct. Mol. Biol.* 25:557–569. https://doi.org/10.1038/s41594-018-0078-9

Ferrandiz, N., C. Barroso, O. Telecan, N. Shao, H.M. Kim, S. Testori, P. Faull, P. Cutillas, A.P. Snijders, M.P. Colaiácovo, et al. 2018. Spatiotemporal

regulation of Aurora B recruitment ensures release of cohesion during C. elegans oocyte meiosis. *Nat. Commun.* 9:834. https://doi.org/10.1038/s41467-018-03229-5

Gao, J., and M.P. Colaiácovo. 2018. Zipping and Unzipping: Protein Modifications Regulating Synaptonemal Complex Dynamics. *Trends Genet.* 34:232–245. https://doi.org/10.1016/j.tig.2017.12.001

Gao, J., C. Barroso, P. Zhang, H.M. Kim, S. Li, L. Labrador, J. Lightfoot, M.V. Gerashchenko, V.M. Labunskyy, M.Q. Dong, et al. 2016. N-terminal acetylation promotes synaptonemal complex assembly in C. elegans. *Genes Dev.* 30:2404–2416. https://doi.org/10.1101/gad.277350.116

Gladstone, M.N., D. Obeso, H. Chuong, and D.S. Dawson. 2009. The synaptonemal complex protein Zip1 promotes bi-orientation of centromeres at meiosis I. *PLoS Genet.* 5:e1000771. https://doi.org/10.1371/journal.pgen.1000771

Gómez, R., N. Felipe-Medina, M. Ruiz-Torres, I. Berenguer, A. Viera, S. Pérez, J.L. Barbero, E. Llano, T. Fukuda, M. Alsheimer, et al. 2016. Sororin loads to the synaptonemal complex central region independently of meiotic cohesin complexes. *EMBO Rep.* 17:695–707. https://doi.org/10.15252/embr.201541060

Goodyer, W., S. Kaitna, F. Couteau, J.D. Ward, S.J. Boulton, and M. Zetka. 2008. HTP-3 links DSB formation with homolog pairing and crossing over during C. elegans meiosis. *Dev. Cell.* 14:263–274. https://doi.org/10.1016/j.devcel.2007.11.016

Harper, N.C., R. Rillo, S. Jover-Gil, Z.J. Assaf, N. Bhalla, and A.F. Dernburg. 2011. Pairing centers recruit a Polo-like kinase to orchestrate meiotic chromosome dynamics in C. elegans. *Dev. Cell.* 21:934–947. https://doi.org/10.1016/j.devcel.2011.09.001

Holloway, J.K., X. Sun, R. Yokoo, A.M. Villeneuve, and P.E. Cohen. 2014. Mammalian CNTD1 is critical for meiotic crossover maturation and deselection of excess precrossover sites. *J. Cell Biol.* 205:633–641. https://doi.org/10.1083/jcb.201401122

Hsu, J.Y., Z.W. Sun, X. Li, M. Reuben, K. Tatchell, D.K. Bishop, J.M. Grushcow, C.J. Brame, J.A. Caldwell, D.F. Hunt, et al. 2000. Mitotic phosphorylation of histone H3 is governed by Ipl1/aurora kinase and Glc7/PP1 phosphatase in budding yeast and nematodes. *Cell.* 102:279–291. https://doi.org/10.1016/S0092-8674(00)00034-9

Humphryes, N., W.K. Leung, B. Argunhan, Y. Terentyev, M. Dvorackova, and H. Tsubouchi. 2013. The Ecm11-Gmc2 complex promotes synaptonemal complex formation through assembly of transverse filaments in budding yeast. *PLoS Genet.* 9:e1003194. https://doi.org/10.1371/journal.pgen.1003194

Janisiw, E., M.R. Dello Stritto, V. Jantsch, and N. Silva. 2018. BRCA1-BARD1 associate with the synaptonemal complex and pro-crossover factors and influence RAD-51 dynamics during Caenorhabditis elegans meiosis. *PLoS Genet.* 14:e1007653. https://doi.org/10.1371/journal.pgen.1007653

Leung, W.K., N. Humphryes, N. Afshar, B. Argunhan, Y. Terentyev, T. Tsubouchi, and H. Tsubouchi. 2015. The synaptonemal complex is assembled by a polySUMOylation-driven feedback mechanism in yeast. *J. Cell Biol.* 211:785–793. https://doi.org/10.1083/jcb.201506103

Li, Q., T.T. Saito, M. Martinez-Garcia, A.J. Deshong, S. Nadarajan, K.S. Lawrence, P.M. Checchi, M.P. Colaiacovo, and J. Engebrecht. 2018. The tumor suppressor BRCA1-BARD1 complex localizes to the synaptonemal complex and regulates recombination under meiotic dysfunction in Caenorhabditis elegans. *PLoS Genet.* 14:e1007701. https://doi.org/10.1371/journal.pgen.1007701

Lupas, A., M. Van Dyke, and J. Stock. 1991. Predicting coiled coils from protein sequences. *Science.* 252(5009):1162–1164. https://doi.org/10.1126/science.252.5009.1162

MacQueen, A.J., M.P. Colaiácovo, K. McDonald, and A.M. Villeneuve. 2002. Synapsis-dependent and -independent mechanisms stabilize homolog pairing during meiotic prophase in C. elegans. *Genes Dev.* 16:2428–2442. https://doi.org/10.1101/gad.1011602

Martinez-Perez, E., M. Schvarzstein, C. Barroso, J. Lightfoot, A.F. Dernburg, and A.M. Villeneuve. 2008. Crossovers trigger a remodeling of meiotic chromosome axis composition that is linked to two-step loss of sister chromatid cohesion. *Genes Dev.* 22:2886–2901. https://doi.org/10.1101/gad.1694108

Moses, M.J. 1969. Structure and function of the synaptonemal complex. *Genetics.* 61(Suppl):41–51.

Nabeshima, K., A.M. Villeneuve, and M.P. Colaiácovo. 2005. Crossing over is coupled to late meiotic prophase bivalent differentiation through asymmetric disassembly of the SC. *J. Cell Biol.* 168:683–689. https://doi.org/10.1083/jcb.200410144

Nadarajan, S., T.J. Lambert, E. Altendorfer, J. Gao, M.D. Blower, J.C. Waters, and M.P. Colaiácovo. 2017. Polo-like kinase-dependent phosphorylation of the synaptonemal complex protein SYP-4 regulates double-strand break formation through a negative feedback loop. *eLife.* 6:e23437. https://doi.org/10.7554/eLife.23437

Newnham, L., P. Jordan, B. Rockmill, G.S. Roeder, and E. Hoffmann. 2010. The synaptonemal complex protein, Zip1, promotes the segregation of nonexchange chromosomes at meiosis I. *Proc. Natl. Acad. Sci. USA.* 107:781–785. https://doi.org/10.1073/pnas.0913435107

Ortiz, M.A., D. Noble, E.P. Sorokin, and J. Kimble. 2014. A new dataset of spermatogenic vs. oogenic transcriptomes in the nematode Caenorhabditis elegans. *G3 (Bethesda).* 4:1765–1772. https://doi.org/10.1534/g3.114.012351

Pak, C.W., M. Kosno, A.S. Holehouse, S.B. Padrick, A. Mittal, R. Ali, A.A. Yunus, D.R. Liu, R.V. Pappu, and M.K. Rosen. 2016. Sequence Determinants of Intracellular Phase Separation by Complex Coacervation of a Disordered Protein. *Mol. Cell.* 63:72–85. https://doi.org/10.1016/j.molcel.2016.05.042

Pattabiraman, D., B. Roelens, A. Woglar, and A.M. Villeneuve. 2017. Meiotic recombination modulates the structure and dynamics of the synaptonemal complex during C. elegans meiosis. *PLoS Genet.* 13:e1006670. https://doi.org/10.1371/journal.pgen.1006670

Phillips, C.M., and A.F. Dernburg. 2006. A family of zinc-finger proteins is required for chromosome-specific pairing and synapsis during meiosis in C. elegans. *Dev. Cell.* 11:817–829. https://doi.org/10.1016/j.devcel.2006.09.020

Phillips, C.M., C. Wong, N. Bhalla, P.M. Carlton, P. Weiser, P.M. Meneely, and A.F. Dernburg. 2005. HIM-8 binds to the X chromosome pairing center and mediates chromosome-specific meiotic synapsis. *Cell.* 123:1051–1063. https://doi.org/10.1016/j.cell.2005.09.035

Qiao, H., J.K. Chen, A. Reynolds, C. Höög, M. Paddy, and N. Hunter. 2012. Interplay between synaptonemal complex, homologous recombination, and centromeres during mammalian meiosis. *PLoS Genet.* 8:e1002790. https://doi.org/10.1371/journal.pgen.1002790

Rog, O., S. Köhler, and A.F. Dernburg. 2017. The synaptonemal complex has liquid crystalline properties and spatially regulates meiotic recombination factors. *eLife.* 6:e21455. https://doi.org/10.7554/eLife.21455

Sato-Carlton, A., C. Nakamura-Tabuchi, S.K. Chartrand, T. Uchino, and P.M. Carlton. 2018. Phosphorylation of the synaptonemal complex protein SYP-1 promotes meiotic chromosome segregation. *J. Cell Biol.* 217:555–570. https://doi.org/10.1083/jcb.201707161

Schild-Prüfert, K., T.T. Saito, S. Smolikov, Y. Gu, M. Hincapie, D.E. Hill, M. Vidal, K. McDonald, and M.P. Colaiácovo. 2011. Organization of the synaptonemal complex during meiosis in Caenorhabditis elegans. *Genetics.* 189:411–421. https://doi.org/10.1534/genetics.111.132431

Schücker, K., T. Holm, C. Franke, M. Sauer, and R. Benavente. 2015. Elucidation of synaptonemal complex organization by super-resolution imaging with isotropic resolution. *Proc. Natl. Acad. Sci. USA.* 112:2029–2033. https://doi.org/10.1073/pnas.1414814112

Smolikov, S., A. Eizinger, K. Schild-Prufert, A. Hurlburt, K. McDonald, J. Engebrecht, A.M. Villeneuve, and M.P. Colaiácovo. 2007. SYP-3 restricts synaptonemal complex assembly to bridge paired chromosome axes during meiosis in Caenorhabditis elegans. *Genetics.* 176:2015–2025. https://doi.org/10.1534/genetics.107.072413

Smolikov, S., K. Schild-Prüfert, and M.P. Colaiácovo. 2009. A yeast two-hybrid screen for SYP-3 interactors identifies SYP-4, a component required for synaptonemal complex assembly and chiasma formation in Caenorhabditis elegans meiosis. *PLoS Genet.* 5:e1000669. https://doi.org/10.1371/journal.pgen.1000669

Stiernagle, T.. 2006. Maintenance of C. elegans. *WormBook.* 1–11. . https://doi.org/10.1895/wormbook.1.101.1

Takeo, S., C.M. Lake, E. Morais-de-Sá, C.E. Sunkel, and R.S. Hawley. 2011. Synaptonemal complex-dependent centromeric clustering and the initiation of synapsis in Drosophila oocytes. *Curr. Biol.* 21:1845–1851. https://doi.org/10.1016/j.cub.2011.09.044

Torrisi, M., M. Kaleel, and G. Pollastri. 2018. Porter 5: state-of-the-art ab initio prediction of protein secondary structure in 3 and 8 classes. *bioRxiv.* doi:https://doi.org/10.1101/289033 (Preprint posted October 5, 2018).

Tung, K.S., and G.S. Roeder. 1998. Meiotic chromosome morphology and behavior in zip1 mutants of Saccharomyces cerevisiae. *Genetics.* 149:817–832.

Tzur, Y.B., C. Egydio de Carvalho, S. Nadarajan, I. Van Bostelen, Y. Gu, D.S. Chu, I.M. Cheeseman, and M.P. Colaiácovo. 2012. LAB-1 targets PP1 and restricts Aurora B kinase upon entrance into meiosis to promote sister chromatid cohesion. *PLoS Biol.* 10:e1001378. https://doi.org/10.1371/journal.pbio.1001378

Tzur, Y.B., E. Winter, J. Gao, T. Hashimshony, I. Yanai, and M.P. Colaiácovo. 2018. Spatiotemporal Gene Expression Analysis of the *Caenorhabditis elegans* Germline Uncovers a Syncytial Expression Switch. *Genetics*. 210: 587–605. https://doi.org/10.1534/genetics.118.301315

Voelkel-Meiman, K., S.S. Moustafa, P. Lefrançois, A.M. Villeneuve, and A.J. MacQueen. 2012. Full-length synaptonemal complex grows continuously during meiotic prophase in budding yeast. *PLoS Genet.* 8: e1002993. https://doi.org/10.1371/journal.pgen.1002993

Woglar, A., and A.M. Villeneuve. 2018. Dynamic Architecture of DNA Repair Complexes and the Synaptonemal Complex at Sites of Meiotic Recombination. *Cell.* 173:1678–1691.e16. https://doi.org/10.1016/j.cell.2018.03.066

Yokoo, R., K.A. Zawadzki, K. Nabeshima, M. Drake, S. Arur, and A.M. Villeneuve. 2012. COSA-1 reveals robust homeostasis and separable licensing and reinforcement steps governing meiotic crossovers. *Cell.* 149:75–87. https://doi.org/10.1016/j.cell.2012.01.052

Yuan, L., J. Pelttari, E. Brundell, B. Björkroth, J. Zhao, J.G. Liu, H. Brismar, B. Daneholt, and C. Höög. 1998. The synaptonemal complex protein SCP3 can form multistranded, cross-striated fibers in vivo. *J. Cell Biol.* 142: 331–339. https://doi.org/10.1083/jcb.142.2.331

Zhang, L., S. Köhler, R. Rillo-Bohn, and A.F. Dernburg. 2018. A compartmentalized signaling network mediates crossover control in meiosis. *eLife.* 7:e30789. https://doi.org/10.7554/eLife.30789

Supplemental material

A SYP-2::GFP mass spectrometry analysis

Locus	Gene name	Size (kD)	Total spectral count
C24G6.1	*syp-2*	23.69	432
F26D2.2	*syp-1*	56.55	160
F57B10.4	*syp-6*	77.6	130
H27M09.3	*syp-4*	67.25	84
Y54E10A.12	*syp-5*	62.53	65
B0281.3	*B0281.3*	37.56	22
F46A9.5	*skr-1*	20.02	14
F37C12.7	*acs-4*	81.2	13
T23H2.1	*npp-12*	199.52	14
D1005.1	*D1005.1*	121.54	13
F25H5.1	*lim-9*	74.05	10
F39H2.4	*syp-3*	25.85	8
Y47D3B.10	*dpy-18*	63.89	7
F59D8.2	*vit-4*	186.19	6
C07A12.4	*pdi-2*	55.12	6
T10B10.2	*ucr-2.2*	44.19	6
C04C11.2	*arrd-25*	64.34	6
R11.1	*R11.1*	31.78	6
F46A9.4	*skr-2*	19.58	5
F08C6.6	*apy-1*	40.29	5

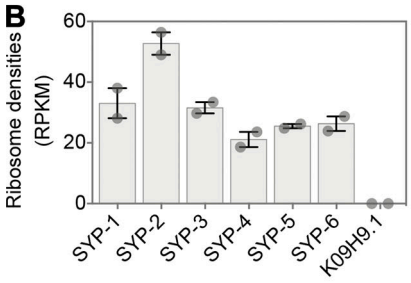

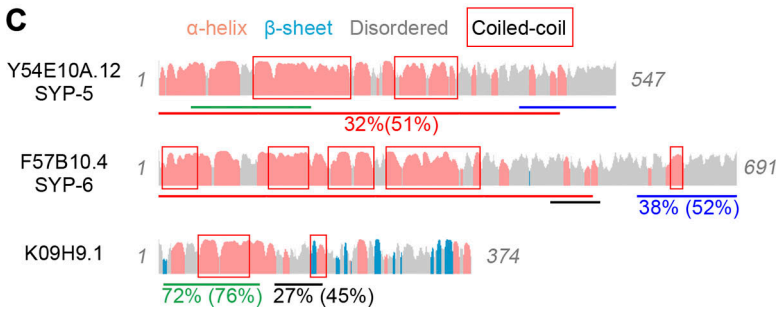

Figure S1. **Identification of SYP-2::GFP binding proteins. (A)** List of SYP-2::GFP binding proteins identified by IP and MS. K09H9.1 is a predicted paralog of SYP-5 and SYP-6, but it was not detected in the immunoprecipitates. **(B)** SYP proteins show comparable translation rates, and the translation of K09H9.1 was not detected (data extracted from Tzur et al. [2018]). Scatter plots with bar graphs depict mean ± SEM of data from two biological replicates. **(C)** Secondary protein structure of SYP-5, SYP-6, and K09H9.1. Lines of the same color represent regions of homology; amino acid identity and similarity (in parentheses) are indicated. These data suggest that K09H9.1 is unlikely to function as a SYP in worms.

D Plate phenotypes

genotype	% viable embryos (# of embryos scored)	% males (# of adults scored)
wild type	100.0 (454)	0.1 (2652)
syp-5(cac1)	79.8 (1089)	9.8 (2357)
syp-6(cac3)	99.2 (584)	1.2 (2530)
syp-5(cac1) syp-6(cac-3)	3.4(1071)	36.1 (36)
syp-5::gfp(cac4)	100.0 (672)	0.6 (1716)
syp-6::gfp(cac5)	100.0 (582)	0.1 (890)
syp-5::gfp(cac4) syp-6(cac3)	90.1 (857)	2.9 (849)
syp-5(cac27) (delC)	81.9 (431)	9.2 (1243)
syp-5(cac34) (syp-6 C)	97.3 (832)	1.5 (2451)
syp-5(cac43) (14K)	93.5 (1182)	3.0 (2467)
syp-4(cac42) (22K)	36.6(982)	28.9 (720)

Figure S2. ***syp* mutants created by CRISPR method in this study. (A)** For *syp-5* gene editing, *syp-5*(*cac1*) (asterisk) is an Indel frameshift mutation that occurs downstream of the initiation codon within the first exon and creates a putative 16-aa protein product. Thus, this mutant was considered to be a null mutant, which was also confirmed by SYP-5 immunostaining in Fig. S5 B. *syp-5::gfp* (*cac4*) (black arrowhead) was created by inserting the coding sequences of the 4-aa linker "GGSG" and the GFP protein before the stop codon. In *syp-5(delC)*(*cac27*) mutant allele, a 1,397-bp genome sequence (red line) was deleted to remove a SYP-5 C-terminal IDR region that contains a CIE cluster. In the *syp-5*(*syp-6 C)*(*cac34*) mutant, a 2,512-bp *syp-5* genomic sequence (green line) that encodes the C-terminal 162-aa region was replaced by a 1,160-bp *syp-6* genomic sequence that encodes the SYP-6 C-terminal 291-aa region. In the *syp-5(14K)*(*cac43*) mutant, point mutations for 14 aa within the SYP-5 C-terminal region were introduced into the *syp-5* genome sequence (within the blue line region). **(B)** For *syp-6* gene editing, *syp-6(cac3)* contained a 2,068-bp deletion mutation, removing the majority of the gene sequence (red line) and resulting in a frameshift of the remaining coding sequence, and this mutant was thus considered a null mutant. *syp-6*(*cac5*) (black arrowhead) was created by inserting the coding sequences of the 4-aa linker "GGSG" and GFP protein before the stop codon. Green line indicates the region used to replace *syp-5* sequence in the *syp-5*(*syp-6 C)* mutant. **(C)** For the *syp-4(22K)*(*cac42)* mutant, point mutations of 22 aa within the SYP-4 C-terminal IDR region were introduced into a 544-bp region in the *syp-4* genome sequence (blue line). **(D)** Plate phenotype analysis for the listed genotypes.

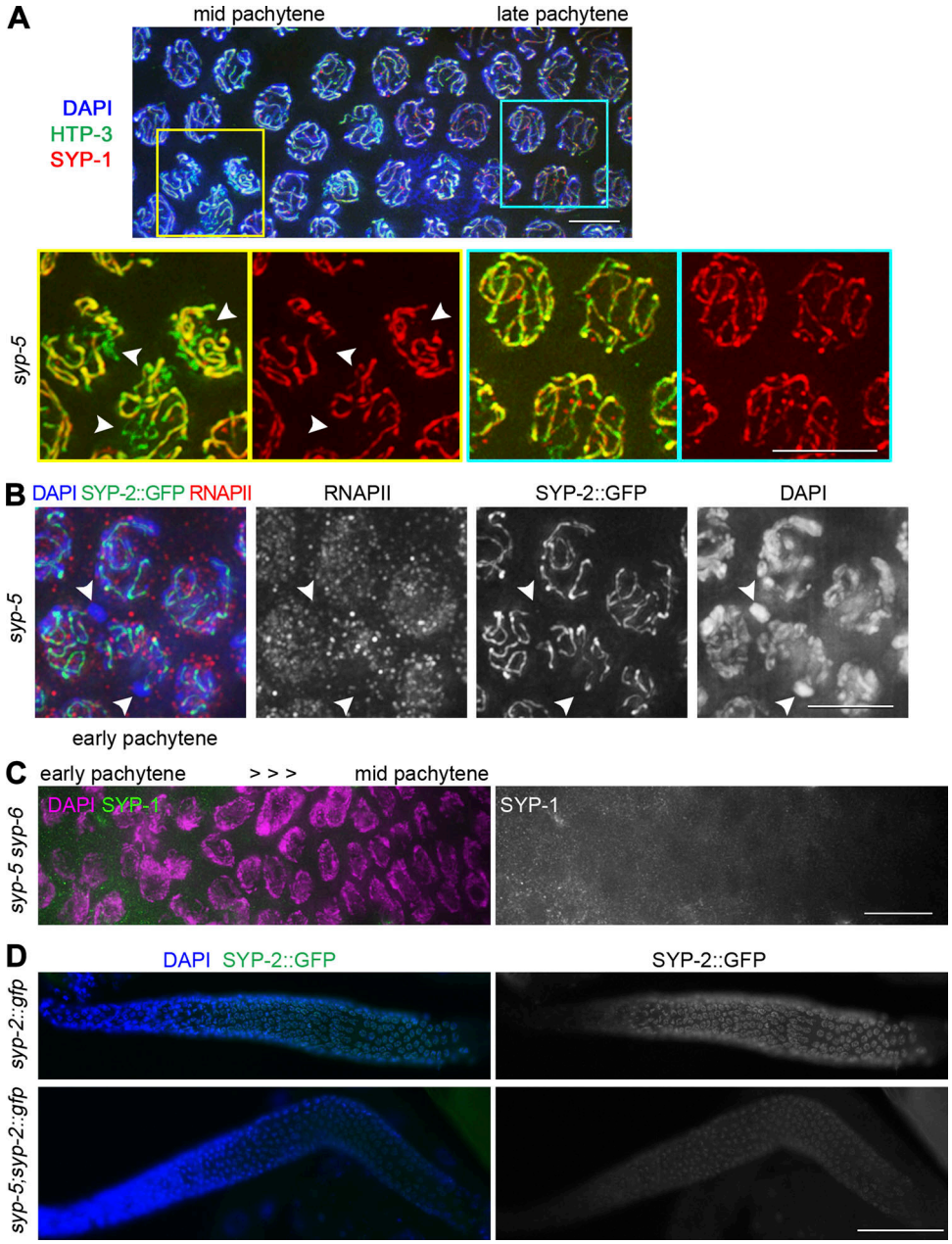

Figure S3. **Analysis of chromosome synapsis in *syp-5* and *syp-5 syp-6* mutants. (A)** Immunostaining of SYP-1 (red) and HTP-3 (green) in mid- to late-pachytene nuclei of *syp-5* mutants. Chromatin was stained with DAPI (blue). Magnified images are shown for the yellow and cyan boxed fields, showing that SC assembly defects (arrowheads) were frequently observed in nuclei at mid pachytene (yellow box) but not during late-pachytene stage (cyan box). Yellow stretches indicate the colocalization of HTP-3 with SYP-1. Bar, 5 µm. **(B)** Immunostaining of RNA polymerase II (RNAPII, red) in early pachytene nuclei of *syp-5; syp-2::gfp* gonads. Chromatin was stained with DAPI (blue). Chromosomes that lack SYP-2::GFP were also devoid of RNAPII (white arrowheads), suggesting that SC assembly is frequently affected on the X chromosomes during the early meiotic prophase, which may be linked to the high Him phenotype of *syp-5* mutants. Bar, 5 µm. **(C)** The SC (visualized by SYP-1 immunostaining, green) was not detected in pachytene nuclei of *syp-5 syp-6* double mutants. Chromatin was stained with DAPI (magenta). Bar, 5 µm. **(D)** Chromosome association of SC central region proteins (as indicated by SYP-2::GFP, green) was reduced in *syp-5* mutant background. Gonads dissected from indicated genotypes were fixed and stained with DAPI (blue). Bar, 50 µm.

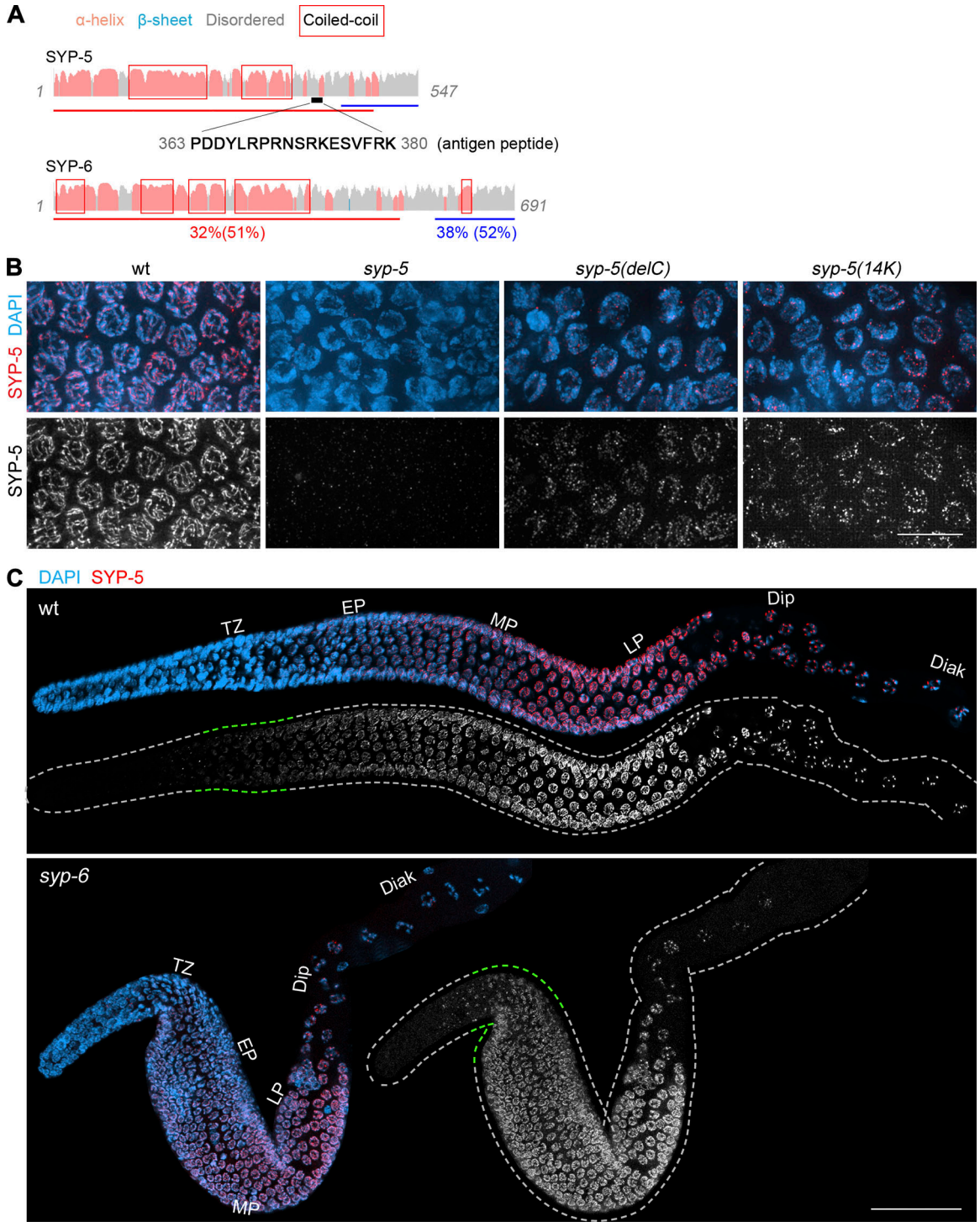

Figure S4. **Analysis of SYP-5 expression by immunostaining with a SYP-5 antibody. (A)** A polyclonal antibody against SYP-5 was produced in rabbits with a synthesized antigen peptide. The schematic diagram shows the location of the antigen peptide within the SYP-5 sequence (black bar). This antigen sequence does not share similarity with SYP-6. Lines of the same color represent regions of homology between SYP-5 and SYP-6. **(B)** Immunostaining of SYP-5 (red) in gonads dissected from the indicated genotypes. Chromatin was stained with DAPI (blue). Continuous SYP-5 staining signals were observed in wild type, but only foci or short stretches were formed in *syp-5(delC)* or *syp-5(14K)* mutants. Bar, 10 µm. **(C)** Immunostaining of SYP-5 (red) in wild type and *syp-6* mutant gonads. Dashed lines depict the outlines of the gonads, and the regions in green dashed lines correspond to the TZ during meiotic prophase. Chromatin was stained with DAPI (blue). Bar, 50 µm. Diak, diakinesis; Dip, diplotene; EP, early pachytene; LP, late pachytene; MP, mid-pachytene; wt, wild type.

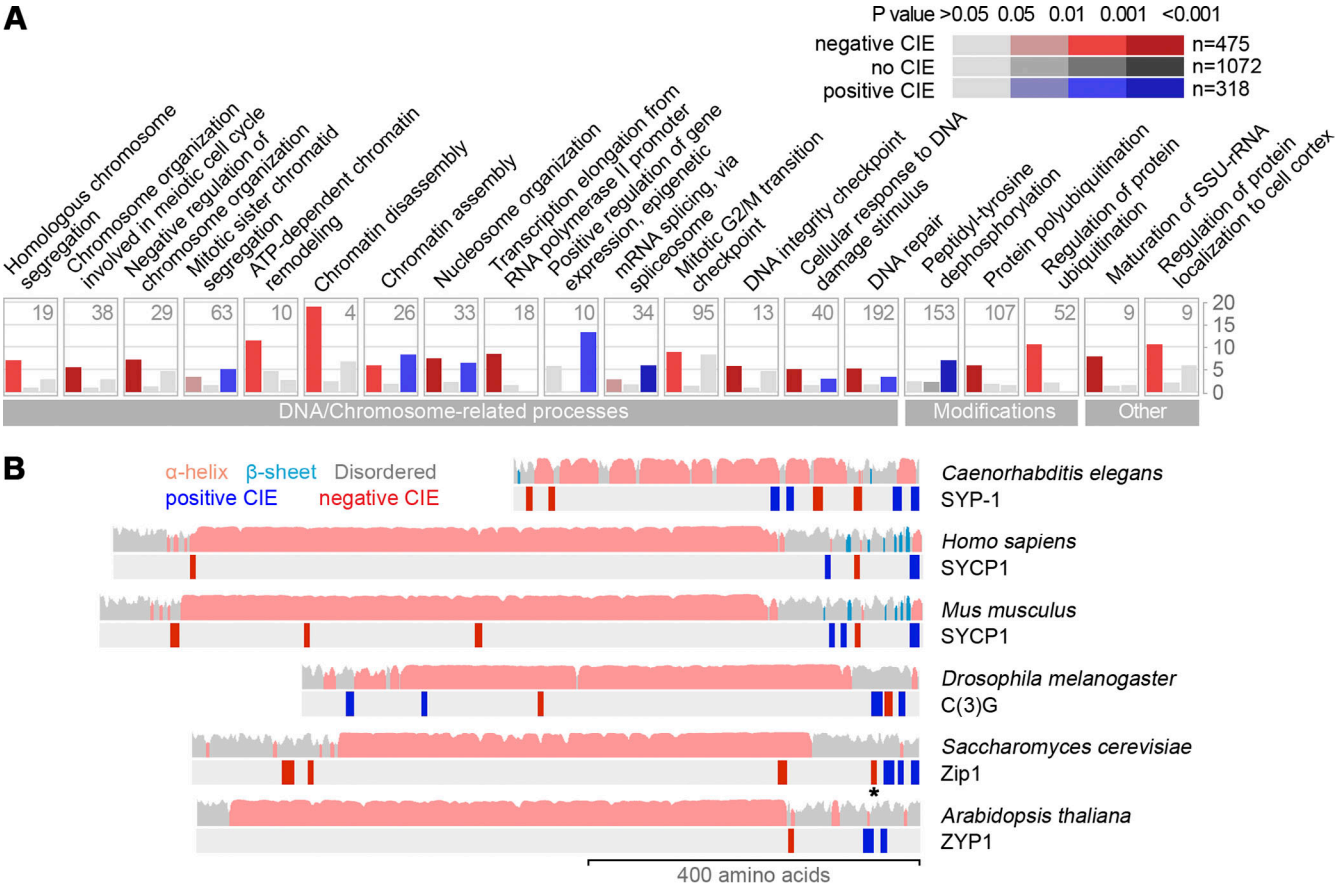

C SC central region components other than TFs

Organism	Protein	AA length	% IDR	CIE(-)	CIE(+)
Caenorhabditis elegans	SYP-2	213	35.7	2	2
	SYP-3	224	9.4	1	0
	SYP-4	605	52.9	7	1
	SYP-5	547	36.0	6	2
	SYP-6	691	44.1	3	3
Homo sapiens	SYCE1	315	26.7	1	0
	SYCE2	212	52.4	1	0
	SYCE3	88	12.5	1	0
	TEX12	123	43.1	1	0
	SIX6OS1	623	57.3	4	0
Drosophila melanogaster	Cona	207	19.8	1	0
	Corolla	552	56.3	6	0
Saccharomyces cerevisiae	Ecm11	302	62.2	2	2
	Gmc2	188	29.3	0	0
	SUMO(poly)	117	65.0	1	0

D SC regulators and clients in worm and fly

Protein	AA length	% IDR	CIE(-)	CIE(+)	Note
AKIR-1	218	67.4	2	1	SC regulator
BRC-1	612	65.2	6	4	SC client
BRD-1	702	60.5	2	4	SC client
HAL-2	308	39.0	2	2	SC regulator
PLK-2	632	51.9	2	2	SC client
ZHP-1	216	50.9	2	1	SC client
ZHP-2	240	50.8	0	1	SC client
ZHP-3	387	55.6	0	1	SC client
ZHP-4	283	50.9	0	1	SC client
Sororin (fly)	857	83.4	8	10	SC client

Figure S5. **Enrichment analysis of CIEs in the *C. elegans* proteome and SC components across organisms. (A)** Gene ontology (GO) analysis of IDR-containing proteins in the *C. elegans* germline proteome. CIE analysis in the germline proteome (Fig. 6 C) identified 475 proteins containing long-range negative CIEs (with 20 aa or longer) in their IDRs and 318 proteins containing long-range positive CIEs, while 1,072 IDR-containing proteins did not have a CIE segment. GO term analysis of these three groups of proteins revealed the enrichment of CIE-containing proteins in specific biological processes. Biological processes with at least threefold differences in protein enrichments between any two groups are shown. The numbers of the reference genes are indicated for each biological process. G2, preparation for mitosis; M, mitosis; SSU-rRNA, small subunit ribosomal RNA. **(B)** CIE distribution among SC TF proteins from various organisms. An in-frame deletion that resulted in the removal of a negative CIE (indicated by an asterisk) from yeast TF protein Zip1 abolished SC assembly (Tung and Roeder, 1998). **(C)** Presence of CIE segments among SC central regional components other than TF proteins. **(D)** Presence of CIE segments on SC regulators and client proteins in *C. elegans* and *D. melanogaster* (gray shading). Red and blue numbers indicate the negative and positive CIEs identified in these proteins, respectively.